

Gearbox Dynamics in the Modeling of Rotating Machinery

A Thesis
Presented to
the faculty of the School of Engineering and Applied Science
University of Virginia

In Partial Fulfillment
of the requirements for the Degree
Master of Science

by

Jason Andrew Kaplan

May 2012

APPROVAL SHEET

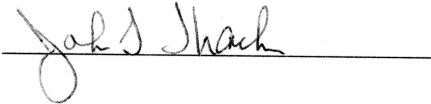
The thesis
is submitted in partial fulfillment of the requirements
for the degree of
Master of Science


AUTHOR

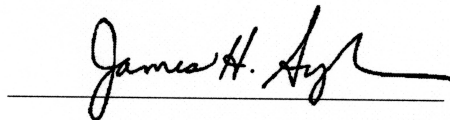
The thesis has been read and approved by the examining committee:


Advisor





Accepted for the School of Engineering and Applied Science:



Dean, School of Engineering and Applied Science

May
2012

Abstract

The ability to accurately predict rotating machine resonant frequencies and to assess their stability and response to external forces is crucial from a reliability and preventive maintenance perspective. Resonant frequencies and forced response become more difficult to predict when additional complicated components such as gearboxes are present in the rotor system. Gearbox dynamics contain many complexities. No computationally straight forward methods are currently available in the literature that relate gear forces and moments acting in 3-D space to the deflections of a wide variety of shaft systems in gear trains. Several models for analyzing gear forces and deflections have been proposed, but they focus primarily on the dynamics of the gearbox itself and neglect vibration transmission through the remainder of the drive-train. More recent models have used the finite element method to couple the lateral and torsional degrees-of-freedom of shaft systems to the forces and moments of the gears through stiffness matrices. However, these models were limited to spur geared systems and could not account for the forces and moments produced by helical gears, which act not only in the lateral and torsional directions but also in the axial direction. A finite element formulation of gearboxes, which couples the axial, lateral, and torsional degrees-of-freedom of the connected shafts, is developed in this thesis. The thesis contains applications to two industrial gear trains. It has the capability to apply to a wide variety of both spur and helical geared systems set at arbitrary orientation angles.

Table of Contents

1. Introduction.....	11
1.1. Problem Statement.....	11
1.2. Summary.....	13
2. Literature Review.....	15
2.1. Dynamic Factor.....	15
2.2. Tooth Compliance Models.....	15
2.3. Gears and Rotor Dynamics.....	19
2.4. Recent Advances.....	22
3. Gear Mesh Analysis.....	27
3.1. Gear Mesh Finite Element Model.....	27
3.2. Derivation of Mesh Stiffness Matrix.....	30
3.3. Incorporation into the Gear Finite Element Model.....	36
4. Industrial Gearbox Application 1.....	39
4.1. Introduction.....	39
4.2. Gearbox Rotor Dynamic Analysis.....	42
4.3. Stability Analysis.....	44
4.4. Bearing Redesign Analysis.....	48
4.5. Unbalance Response.....	54
4.6. Conclusion.....	60

5. Industrial Gearbox Application 2	61
5.1. Introduction.....	61
5.2. Full Shaft Finite Element Model of Drive-train 2.....	63
5.3. Bearings.....	69
5.4. Flexible Couplings.....	70
5.5. Gearbox.....	71
5.6. Natural Frequencies and Mode Shape Summary.....	72
5.7. Conclusion.....	80
6. Conclusions	83
6.1. Accomplishments.....	83
6.2. Implications.....	85
6.3. Future Work.....	86

List of Figures

Figure 1.1.1: Automotive gearbox.....	11
Figure 1.1.2: PW-1000G Geared-turbofan jet engine.....	11
Figure 2.2.1: Tuplin's gear tooth model.....	16
Figure 2.2.2: Torsional gear model.....	17
Figure 2.2.3: Finite element model of single spur tooth.....	18
Figure 2.3.1: Lateral-torsional coupled model of shaft-gear system.....	20
Figure 3.1.1: Gear mesh finite element representation.....	29
Figure 3.2.1: Gear forces and parameters.....	33
Figure 3.2.2: Gear pair orientation angle.....	33
Figure 3.3.1: Finite element representation of a geared system.....	36
Figure 4.1.1: Steam-turbine generator model.....	39
Figure 4.1.2: Spectrum plot of HS shaft at 10,201 RPM.....	40
Figure 4.2.3: Gearbox finite element beam model.....	43
Figure 4.3.1: Eigenvalue comparison of mode.....	48
Figure 4.4.1: Stiffness and damping coefficients vs load.....	49
Figure 4.4.2: Eccentricity plot.....	50
Figure 4.4.3: Pressure profile plot load case 1.....	51
Figure 4.4.4: Pressure profile plot load case 5.....	52
Figure 4.4.5: Pressure profile plot load case 10.....	52
Figure 4.4.6: Eccentricity plot min and max clearances.....	53
Figure 4.4.7: Stiffness and damping min and max clearance.....	54
Figure 4.5.1: Unbalance response, load case 1, min clearance.....	56

Figure 4.5.2: Unbalance phase, load case 1, min clearance.....	56
Figure 4.5.3: Unbalance response, load case 5, min clearance.....	56
Figure 4.5.4: Unbalance phase, load case 5, min clearance.....	57
Figure 4.5.5: Unbalance response, load case 10, min clearance.....	57
Figure 4.5.6: Unbalance phase, load case 10, min clearance.....	57
Figure 4.5.7: Unbalance response, load case 1, max clearance.....	58
Figure 4.5.8: Unbalance phase, load case 1, max clearance.....	58
Figure 4.5.9: Unbalance response, load case 5, max clearance.....	58
Figure 4.5.10: Unbalance phase, load case 5, max clearance.....	59
Figure 4.5.11: Unbalance response, load case 10, max clearance.....	59
Figure 4.5.12: Unbalance phase, load case 10, max clearance.....	59
Figure 5.1.1: Drive-train 2 schematic.....	61
Figure 5.1.2: Calculated torsional mode shapes.....	62
Figure 5.2.1: Finite element discretization of drive-train 2.....	63
Figure 5.2.2: Finite element discretization of drive-train 2 LS Shaft.....	64
Figure 5.2.3: Finite element discretization of drive-train 2 HS Shaft.....	65
Figure 5.6.1: Damped mode 1.....	74
Figure 5.6.2: Damped mode 2.....	74
Figure 5.6.3: Damped mode 3.....	75
Figure 5.6.4: Damped mode 4.....	75
Figure 5.6.5: Damped mode 5.....	75
Figure 5.6.6: Damped mode 6.....	76
Figure 5.6.7: Damped mode 7.....	76
Figure 5.6.8: Damped mode 9.....	77

Figure 5.6.9: Damped mode 17.....	78
Figure 5.6.10: Damped mode 23.....	78
Figure 5.6.11: Damped mode 43.....	79
Figure 5.6.12: Damped mode 56.....	79
Figure 5.7.1: Twist comparison of mode 9.....	80
Figure 5.7.2: Twist comparison of mode 17.....	81
Figure 5.7.3: Twist comparison of mode 23.....	81

List of Tables

Table 4.2.1: Generator load cases.....	43
Table 4.3.1: Gearbox properties.....	45
Table 4.3.2: Eigenvalues evaluated with original bearings.....	47
Table 4.3.3: Eigenvalues evaluated with redesigned bearings.....	47
Table 4.4.1: Three-lobe pressure dam pad geometry.....	49
Table 4.4.2: Three-lobe pressure dam geometry.....	49
Table 4.4.3: Three-lobe pressure dam sensitivity analysis.....	53
Table 5.2.1: Drive-train2 Rotor 1 shaft and mass properties.....	66
Table 5.2.2: Drive-train 2 Rotor 2 shaft and mass properties.....	67
Table 5.2.3: Drive-train 2 Rotor 3 shaft and mass properties.....	67
Table 5.2.2: Drive-train 2 Rotor 4 shaft and mass properties.....	69
Table 5.6.1: Drive-train 2 natural frequencies.....	72
Table 5.7.1: Drive-train 2 torsional natural frequency comparison.....	80

Nomenclature

b – Gear tooth face width

C – Damping matrix

d – Horizontal distance between shaft centers

E – Elastic Modulus

f – External force vector

G – Gyroscopic matrix

b – Vertical distance between shaft centers

K – Stiffness matrix

M – Inertia matrix

u – Displacement vector

α – Gear tooth normal pressure angle

β – Gear tooth helical angle

δ – Log decrement

ζ – Damping ratio

φ – Gear direction cosine

φ – Gear orientation angle

ω_n – Natural frequency, rad/s, rpm, Hz

Ω – Rotational speed or excitation frequency, rad/s

Subscripts

i – Node number

j – Node number

x – Horizontal displacement

y – Vertical displacement

ξ – Axial displacement

Chapter 1 Introduction

1.1 Problem Statement

The ability to accurately predict rotating machine resonant frequencies and to assess their stability is crucial from a reliability and preventive maintenance perspective. Resonant frequencies and forced response become more difficult to predict when additional complicated components such as gearboxes are present in the rotor system. Gearing has existed since the beginnings of rotating machinery and yet many aspects of its dynamics remain to be understood. Gearbox dynamics are important to understand because they are prevalent in a wide variety of rotating machines and can substantially transmit and excite vibrations throughout the whole rotor system. Applications of gears to rotary systems include automobile transmissions, geared-turbofan jet engines, wind turbines, and all other power transmission applications that require torque- speed conversions. Examples of an automotive gearbox and a geared-turbofan jet engine are shown in Figures 1.1.1 and 1.1.2.

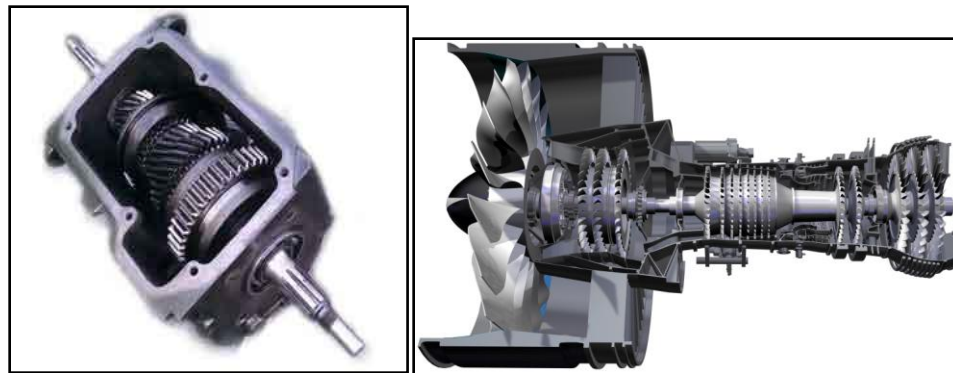


Figure 1.1.1. Automotive gearbox. <http://www.carsparefinder.co.uk/Car-gearbox.htm>.

Figure 1.1.2. PW-1000G Geared-turbofan jet engine <http://www.purepowerengine.com/photos.html#19>

No computationally straight forward methods are available in the literature to relate gear forces and moments acting in 3-D space to the deflections of a wide variety of shaft systems. Several models for analyzing gear forces and deflections have been proposed, but they focus primarily on the dynamics of the gearbox itself and neglect the interactions with the shaft system [37]. More recent models have suggested that the finite element method is the most convenient way to couple the lateral and torsional degrees-of-freedom of the shaft system to the forces and moments of the gears through stiffness matrices [39]. However, these studies were limited to spur gear dynamics and could not account for the forces and moments produced by helical gears, which act in 3-D space.

A finite element formulation of gearboxes, which allows for the coupling of axial, lateral, and torsional degrees-of-freedom of the connected shafts, is proposed in this thesis. The coupling of the degrees-of-freedom at the gear mesh is modeled as a 12x12 stiffness matrix and was originally proposed by Stringer [52]. In this thesis, the gear mesh stiffness matrix is modified and integrated into a rotor dynamic finite element software that solves free and forced vibration models. The applications extend to a wide variety of both spur and helical geared systems.

Gearbox dynamics contain many complexities that include but are not limited to transmission errors resulting from tooth profile errors, elasto-hydrodynamic lubrication (EHL) effects, and time-varying, non-linear forces resulting from gear body or tooth displacements and velocities. Despite the increased accuracy that would result from including these effects in the modeling of gearbox dynamics, they are secondary in importance to incorporating the coupling of the degrees-of-freedom [39].

1.2 Summary

This thesis provides advances in the transition from elementary gear dynamic analyses in the 1920s to modern advanced methods used in geared rotor dynamics. Chapter 2 provides an overview of the history of the methods used in gear dynamic analyses, which form the basis to describe the differences between previous methods and those presented in Chapter 3.

Chapter 3 describes the use of Stringer's 12x12 stiffness matrix to couple the degrees of freedom of a pair of geared parallel shafts and is robust enough to account for arbitrary angles of orientation between them [52]. The theory is extended through its incorporation into a finite element program that has been shown to accurately model the mass, stiffness, gyroscopic, and damping properties of shafts, bearings, disks, and seals. Axial, torsional, and lateral degrees-of-freedom are included for the first time. The advantage of such an implementation is that the modeling of geared systems is generalized so that they will remain accurate for a wide variety of geared drive-trains.

Chapter 4 demonstrates the utility of the gear mesh finite element in accurately modeling the source of sub-synchronous instability in a steam-turbine-generator geared system. The gearbox modeling was useful for determining whether the recommended solution would stabilize the geared drive-train. Subsequent reports indicated that the recommended solution successfully eliminated the unstable sub-synchronous mode and retained the stability of all other modes within the operating speed. Those reports validated the accuracy of incorporating the gear mesh finite element into the analyses.

Chapter 5 models a synchronous motor-compressor geared system and uses the gear mesh finite element to determine its damped natural frequencies and mode shapes for preventive maintenance purposes. The lateral, torsional, and axial coupling inherent in the

gearbox modeling is more accurate than solving the individual non-coupled equations of motion since it predicts modes that the non-coupled equations would miss.

Chapter 2 Literature Review

2.1 Dynamic Factor

This section will explore the foundation of gear dynamics research and its evolution into modern geared rotor dynamic analyses. Gear dynamics have been systematically studied since the 1920s and early 1930s. The objectives in gear dynamic analyses are vast and include models of the following phenomena: bending and contact stresses; scoring and pitting; transmission efficiency; noise radiation; loads on other machine components; system natural frequencies; stability regions; rotor whirl; reliability; and life [37]. The first models focused solely on determining dynamic loads acting on gear teeth through analytical and experimental methods. The purpose of these early studies was to determine the dynamic stresses at the gear roots and to therefore obtain gear life estimates. These studies determined that dynamic loads were not just influenced by pitch line velocities but also by tooth errors and the inertias of the gear and pinion. The inclusion of vibratory models in the dynamic analysis of gears allowed for the investigation of additional dynamic properties.

2.2 Tooth Compliance Models

Computationally straight forward mass-spring dynamic models of gears which included the compliance of gear teeth emerged in the 1950s and early 1960s and served as the first transition between analyzing tooth dynamic loads and accounting for the compliance of several gear components [37]. The models that fit within this category assume that compliance is limited to the gear tooth and that all other components are rigid. Various analyses assumed the gear mesh stiffness to be constant in time or to have time-

varying properties of sinusoidal or rectangular waves. Manufacturing errors, variation in tooth stiffness, and non-linearity in tooth stiffness from loss of contact were attributed to be the three main internal sources of vibration and were incorporated into many of these models in the form of periodic input displacements at the gear mesh location [2]. Despite the simplistic nature of these single DOF models, they could predict dynamic instabilities due to parametric excitations of the gear mesh and from varying the mesh stiffness [6]. An example is shown below in figure 2.2.1 and is one of the first models to investigate the effects of gear error on the dynamic loading of gear teeth. Gear error disturbances were introduced into the model by vertically displacing the wedge. Another classical example of a tooth compliance model is shown below in figure 2.2.2. Torsional vibration is considered and the stiffness and damping of the teeth are represented by a spring and dashpot pair. Gear error is introduced into the model in the form of a displacement input at the mesh.

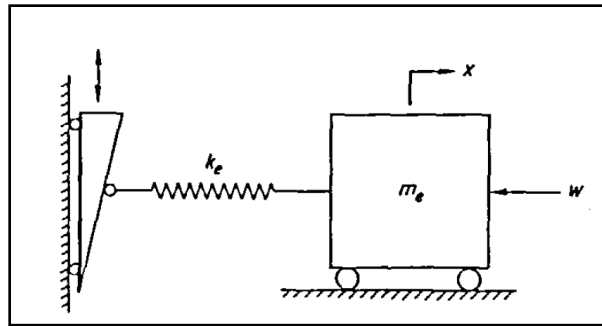


Figure 2.2.1. Spring-mass model created by Tuplin to investigate the effects of gear error on dynamic loading of teeth. The gear error is introduced into the model through vertical displacements of the wedge. K_e =equivalent constant tooth mesh stiffness; m_e =equivalent mass; w =transmitted load. [37]

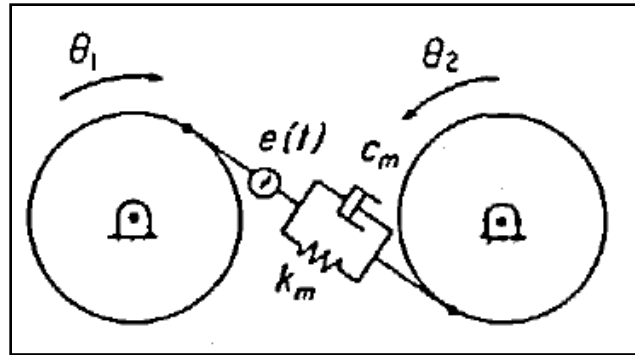


Figure 2.2.2. Torsional model of gears in mesh with constant stiffness, damping, and a displacement input representing gear error. K_m =tooth mesh stiffness; C_m =tooth mesh damping; $e(t)$ =displacement input for gear error. [37]

Additional models of tooth compliance emerged in the 1970s and were the first to include the finite element method. This was a significant departure from treating the gears as lumped inertias and the gear teeth as massless springs since the problem could be formulated much closer to a continuum. Lin, Huston, and Coy investigated the differences in the results obtained using Timoshenko beam and finite element models and discovered that they were substantial for stubby tooth forms [25]. One study used the finite element method to study the effects of dynamic loading on the stress, deformation, and fracture in gear teeth [11]. Wang and Cheng used the finite element method solely to determine the variable tooth stiffness of involute spur gears to then be included in a single DOF lumped model [20]. Their finite element analysis was used to generate a set of curves relating dimensionless tooth stiffness to the number of gear teeth and the loading position throughout the mesh cycle as shown in Figure 2.2.3. The dimensionless tooth stiffness was a function of Young's modulus, load per unit face width, and the root radius of the gears. Figure 2.2.3 also shows the finite element mesh used to generate the family of dimensionless stiffness curves.

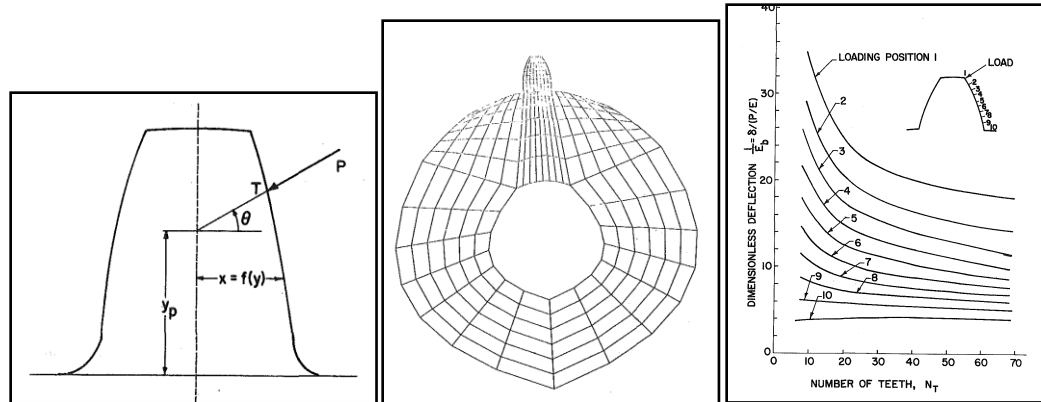


Figure 2.2.3. Finite element modeling and mesh of a single spur tooth. Results indicate the variation of dimensionless deflection with the number of teeth under different contact loading positions indicative of a mesh cycle [20].

Second order effects such as damping and friction appeared in several of these models. Umezawa, Sato, and Kohno modeled the compliance of spur gear teeth as three trapezoidal beams where they determined the bending deflection, shear deflection, and stamp effect at the base of the tooth using Ishikawa's equation (Ishikawa, 1951). They also determined the Hertzian or contact deflection using Weber and Banaschek's equation [26]. Alternative forms of error such as those in the pressure angle, normal pitch, and tooth profile were included in their model and the simulation results for natural frequencies showed good agreement with experimental values. Despite the increases in the complexity of tooth compliance models using finite element analysis, the results showed little differences from those of the pioneering simple mass-spring category with the exception of high-speed cases [37]. Researchers determined, however, that more general models that incorporate the flexibility of other machine components were necessary for several practical applications. Vibration coupling between the gears and their respective shafts and bearings could no longer be neglected when they have comparable stiffnesses.

2.3 Gears and Rotor Dynamics

The effects of gearing on the lateral behavior of shafts were considered in gear dynamics problems in the late 1960s and early 1970s [37]. It was determined that experimental agreement existed for the earlier models because the experiments were designed to satisfy the assumptions of the models regarding the flexibility of the gear teeth relative to the shafts and bearings. These assumptions were often valid for cases where the geared shafts were short and thick but would fail for longer and more slender shaft components. These discoveries prompted the rise for more general gear models and represent the beginnings of gear dynamics where the lateral and torsional degrees of freedom of the shafts are coupled with those of the gears. Several models, however, are simply torsional and account only for the torsional stiffness of the geared shafts [4, 10, 13, 18]. Others include both torsional and lateral motions and consider the torsional and lateral stiffnesses of the geared shafts [12, 15, 14]. Other studies ignore the flexibility of the gear teeth and construct torsional models of rigid gears while the shafts were considered flexible [9, 30]. Their emphasis was placed less on the gear dynamics and more so on the dynamics of the connected shafts and their interactions with the bearings. An example of a laterally and torsionally coupled model is shown in figure 2.3.1. The shafts have torsional stiffness, and the gears have tooth mesh stiffness and lateral stiffness contributions from the shafts and bearings. Mass moments of inertia of the prime mover, load, and the gears are also included in this model.

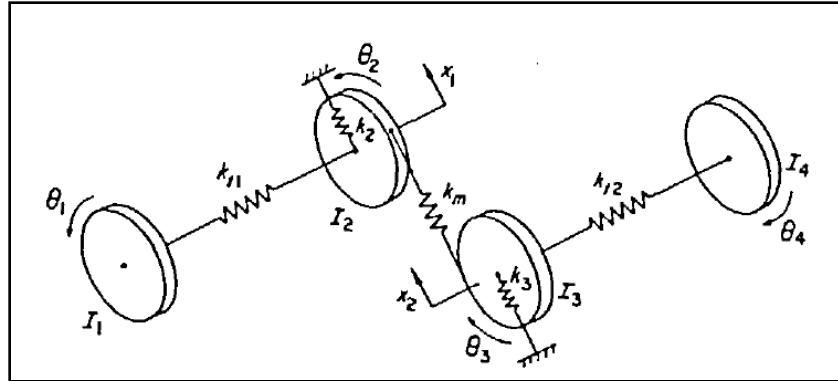


Figure 2.3.1. Laterally-torsionally coupled model of a shaft-gear system. I_1 , and I_4 =mass moment of inertia of prime mover and load; I_2 , and I_3 =mass moment of inertia of gears; K_{1i} =torsional stiffness of shaft i ; K_m =tooth mesh stiffness; K_2 , and K_3 =lateral stiffness representing shaft and bearing flexibility [37].

Several innovations in gear dynamics emerged in the 1970s and 1980s. Models for 3-D stiffness of gear teeth, and non-linear behavior of system elements such as bearings and gear backlash emerged. In addition, friction models of gear teeth included damping and excitation forces. In the late 1980s, developments in axial, lateral, torsional, and plate mode vibrations of geared systems emerged. Both steady state and transient system responses resulting from many variations of gear errors and time-varying mesh stiffness were considered. Johnson's model replaced a varying mesh stiffness by a constant one equal to its mean value and was one of the first attempts at using the gear mesh stiffness to couple the vibration of gear shafts [3]. Kiyono et al focused on constructing helical gear models to compare the results with those of spur gears [16]. They included torsional, lateral, and axial degrees of freedom and treated the gear mesh stiffness as constant. Troeder developed a helical gear pair-shaft-bearing system which involved a torsional, lateral, and axial vibration model where the tooth mesh stiffness was approximated by a Fourier expansion in the form of a square-wave [22]. Kucukay incorporated axial, lateral, and torsional vibration for single-stage helical and spur gear pairs with periodic tooth mesh stiffness, tooth errors, external torques, load dependent contact ratio, and non-linearities from the separation of gear teeth

[27]. Kucukay's results indicated that linear model approximate solutions for the steady-state tooth displacements and loads varied negligibly from the non-linear ones. Ozguven produced a six degree of freedom non-linear model of a spur geared system with time-varying mesh stiffness [38]. The spur geared system consisted of a prime mover, pinion, gear, and load and the degrees of freedom corresponded to four angular rotations of all components and two translations of the gear and pinion just along the line of action. Several factors were explored such as damping, tooth separation, backlash, single and double-sided impacts, and various gear errors (pitch, profile, and run-out). A forced response analysis to internal excitations was conducted and demonstrated the effects of the shaft and bearing dynamics on the gear dynamics.

Mathematical models for geared rotor dynamics emerged in the 1960s as researchers sought to consider the whirling behavior of gear-carrying shafts which required lateral analyses in two mutually perpendicular directions. Although the models in the previous group for geared dynamics considered lateral vibration, the motion was usually restricted to one direction along the line-of-action (LOA). Daws and Mitchell constructed a three-dimensional model of gear coupled rotors in which they used a time-varying stiffness tensor to model the variable mesh stiffness [23]. The interaction between the time varying stiffness and gear deflections was used to predict the forced response of the coupled gear rotors to excitations from mesh errors and unbalanced rotors. Another set of studies examined the free and forced vibration of geared shafts using constant and periodically varying tooth mesh stiffness [28]. The forced response was originally due to mass unbalance but was later extended to include tooth profile errors. These studies used the transfer matrix method for computational efficiency especially when the models included non-linear dynamics.

2.4 Recent Advances

Additional geared rotor dynamic models emerged that incorporate the finite element method to couple the degrees of freedom of connected geared shafts. Neriya, Bhat, and Sankar modeled each gear as a set of two masses, two springs, and two dampers where one set represented the gear and the other a tooth [32]. The shafts were modeled as finite elements and the torsional-lateral coupling could be conveniently introduced at the gear pair locations in the form of stiffness and damping matrices. They assumed constant mesh stiffness and conducted a free vibration analysis to determine the undamped natural frequencies of the linear system. These undamped modes would then be used to calculate the forced response vibration due to mass unbalance and gear eccentricity. They concluded that predictions of geared rotor dynamic behavior, such as critical speeds, mode shapes, and stability onset, are more accurately modeled in finite element analyses when lateral and torsional motions are coupled instead of uncoupled. These results, however, were limited to simple spur-geared systems.

Luo produced a general finite element based model of multi-stage and multi-mesh geared rotor systems that incorporates axial, lateral, and torsional coupling which is applicable to both spur and helical geared systems [42]. A modal synthesis technique was employed so that the model may have a large number of degrees of freedom without the need for a large amount of computer memory. The researchers used a gear transmission in an aircraft engine as an example and showed the axial, lateral, and torsional coupling of modes which is in general agreement with field observations.

Lin and Parker developed a systematic method to analyze the effects of mesh stiffness variations on the instabilities of two-stage spur geared systems [46]. The variations

in mesh stiffness would come from altering the following: mesh frequencies, time-varying mesh stiffness amplitude, contact ratio, and mesh phasing. The two gear mesh stiffnesses were modeled as having mean and time-varying components, where the time-varying parts are periodic at their respective mesh frequencies and are expressed in Fourier series. Analytical solutions were obtained for rectangular waveform tooth mesh stiffnesses and support the notion that perturbations in contact ratio and mesh phasing substantially eliminate or decrease the size of instability regions. Other findings suggest that the excitations originating from one gear mesh may interact substantially with those of the other especially when their frequencies are integer multiples of the other.

Cai develops a vibration model for involute helical gear pairs that incorporates contact ratio, tooth surface errors in the form of shaft deviation and pressure angle errors, and non-linear tooth separation phenomena [41]. A modified stiffness function was produced for a free vibration analysis of the gear pair that includes the effects of addendum modification coefficients, and number of teeth. The dynamic equations of motion are solved using the finite difference method on a 16-bit computer and yield results similar to the experiments and simulations of previous researchers such as Umezawa [26].

Brauer derived a mathematical set of equations describing the shape of conical involute gears and three other types to be used in finite element models [48]. His work was a significant improvement over previous geometric gear models in CAD programs which required large amounts of computational time to generate highly accurate tooth surfaces. The use of equations to define the tooth surfaces not only presented a quicker method to generate the gear model and its elements but is also more robust. Li, Chiou, et al. developed a module that integrates finite element analysis of gear bodies with gear design optimization [45]. This module offered an automatic design optimization routine using interfacial

programs that connected programs that accomplish pre-processing, finite element analysis, and optimization. Consequently, this significantly shortened the procedure of rebuilding gear models through CAD programs to search for an optimal design that satisfies stress/strain requirements obtained from FEA.

Chowdhury produced a model of a helical gear pair mounted on two flexible shafts with rigid bearings using Hamilton's principle [53]. The shafts were modeled as continua with torsional and lateral flexibility while the gears were treated as rigid disks connected by laterally-torsionally coupled mesh springs with time-averaged stiffness. Free vibration analyses of the partially discrete, partially continuous geared system were performed using Galerkin discretization to evaluate eigenvalue sensitivities to rotational speed, and gear mesh stiffness. Forced response analyses due to the effects of static transmission error were conducted using modal analysis.

Kahraman et al developed a finite element model of a spur-gear rotor system with flexible shafts and bearings with degrees of freedom in the lateral and torsional directions [39]. The tooth mesh stiffness is modeled as a spring and damper, with constant stiffness and damping, along the pressure line and is used to produce gear mesh stiffness and damping matrices. Variable mesh stiffness effects were modeled by using a displacement excitation originating at the mesh. These mesh matrices would be added to the uncoupled rotor matrices to complete the global matrices. Critical speeds, mode shapes, and the system forced response to gear mass unbalance, runout, and static transmission error were evaluated. Kahraman et al concluded that the relative compliance of the shaft and the bearings greatly influence not only the mode shapes and natural frequencies but also the dynamic tooth load.

Sun derived a new analytical formula to calculate the bending deformation of involute helical gear teeth using more realistic assumptions of the tooth profile, mass, and load distributions [54]. He divides the tooth section into multiple copies along the spiral angle direction and considers the variable cross-section moment of inertia due to the changing tooth profile, and the variable contact distribution caused by the changing length of the contact line. This method was applied to a helical gear pair example and the results were compared with those of finite element analysis and Ishikawa's method [1]. The results indicated that Sun's analytical formula more closely represented those of FEA than previous formulas such as Ishikawa's.

Stringer developed the methodology for generating a 12x12 gear mesh stiffness matrix that couples the axial, lateral, and torsional degrees of freedom of geared-rotor systems and is therefore applicable to both spur and helical gears [52]. The stiffness matrix is derived from force balances taken along the line of action (LOA) using the Influence Coefficient method, and it incorporates the effects of the normal pressure angle, helical angle, and the arbitrary orientation of the meshing gears. This arbitrary orientation angle of the meshing gears offers a significant advantage over other gear mesh finite element methodologies since it is applicable to complicated gear models where a convenient choice of axes may not be available. A model of a spur-geared-rotor system and bearings is used as an example, and it includes gyroscopic forces and the effects of bearing stiffness and damping properties. The results indicate that the inclusion of the stiffness matrix produces many of the same natural frequencies and modes of the non-geared system but also produces additional ones that represent laterally and torsionally coupled modes. The methods used in Stringer's work are very general and are useful in the creation of broader rotor dynamic models where the gear mesh is one of many substructures.

This thesis expands upon Stringer's work by incorporating his gear mesh stiffness matrix into a rotor dynamic steady-state finite element analysis that accounts for the effects from gyroscopic forces, bearings, disks, squeeze film dampers, and seals in free vibration analyses with axial, lateral, and torsional degrees of freedom. In addition, a simple analog formula used to find tooth-to-tooth contact stiffness, originally developed by Spotts, is used and modified to compute the average gear mesh stiffness, an important parameter in Stringer's 12x12 matrix [31]. The advantages of using this analog formula are that it is computationally efficient while remaining reasonably accurate, and that the user does not require experimental data which may be unavailable or time-consuming to acquire. Most importantly, the ability to accurately model the compliances and degrees of freedom of several other components and sub-structures offers the advantage of solving a wide variety of geared rotor dynamics problems in which the validity of certain simplifying assumptions may be questionable. Incorporating Stringer's research into this finite element analysis will create many opportunities for adding secondary effects due to elasto-hydrodynamic lubrication (EHL), tooth profile error, transmission error, time-varying stiffness, and non-linear forces. Chapter 3 will show the derivation of the 12x12 gear mesh stiffness matrix and will illustrate how it is incorporated into a simple geared-rotor model.

Chapter 3 Gear Mesh Analysis

3.1 Gear Mesh Finite Element Model

This chapter explores the finite element formulation of the inclusion of gearbox dynamics into rotor dynamics. It is based upon a finite element code that uses 2-D Timoshenko beam models for shafts and can easily incorporate bearings, disks, and seals into the equations of motion [51]. Beam elements are widely used to model rotors as they have been shown to produce accurate results when compared to experimental data. The method performs steady-state rotor dynamic analyses and has lateral, torsional, and axial degrees of freedom. Incorporating Stringer's derivation of a 3-D gear mesh stiffness matrix and Spott's model of finite contact stiffness of meshing gear teeth into this finite element code will promote the ability to solve geared rotor dynamics problems with coupled degrees of freedom. Solving the rotor dynamic equations of motion with coupled degrees of freedom are necessary for geared rotor dynamics and will produce more accurate results than solving the individual non-coupled ones.

The approach models the effects of gears, and gear mesh stiffness on the vibration characteristics of rotating machines using the finite element method. The gears will be treated as a pair of rigid lumped masses and inertias that influence the mass, gyroscopic, and stiffness properties of the corresponding shaft nodes in the finite element matrices. The forced response rotor dynamic equations of motion for the entire system model can be represented by the following matrix equation.

$$\mathbf{M}\ddot{\mathbf{u}} + (\mathbf{C} + \mathbf{\Omega}\mathbf{G})\dot{\mathbf{u}} + \mathbf{K}\mathbf{u} = \mathbf{f} \quad (3.1.1)$$

As defined in the Nomenclature, \mathbf{M} represents the inertia matrix, \mathbf{C} represents the damping matrix, \mathbf{G} represents the gyroscopic matrix, $\mathbf{\Omega}$ represents the shaft speed matrix, and \mathbf{K} represents the stiffness matrix. In the free vibration models, the external force vector, \mathbf{f} , is set to $\mathbf{0}$. The effects of the gears and the gear mesh will significantly contribute to the global mass, speed, gyroscopic, and stiffness matrices. The gear mesh lubricant stiffness and damping effects are neglected as well as the excitation forces resulting from profile and static transmission error. These effects must be accounted for in future models.

The mass and gyroscopic contributions to the global matrices are treated the same as those of lumped disks at the nodes of the gear and pinion in rotor dynamics models and therefore will not be emphasized. The elements of the speed matrix, $\mathbf{\Omega}$, will differ for the nodes of shafts that rotate at different speeds because of non-unity gear ratios. The gear mesh effective lateral, torsional, and axial stiffness is modeled as a 12x12 matrix that relates the gear mesh forces and moments, or generalized forces, with each of their respective degrees of freedom. This gear mesh finite element was previously documented in Stringer [52]. It consists of two nodes, i and j , respectively as shown in Figure 3.1.1, where the nodes designate the location of the gear or pinion on the parallel connecting shafts. Each node has six degrees of freedom, which consists of three translations and three angular displacements. The incorporation of this axially, laterally, and torsionally coupled mesh stiffness finite element will provide more accurate displacement solutions for a geared system in a free vibration or forced response rotor dynamic analysis.

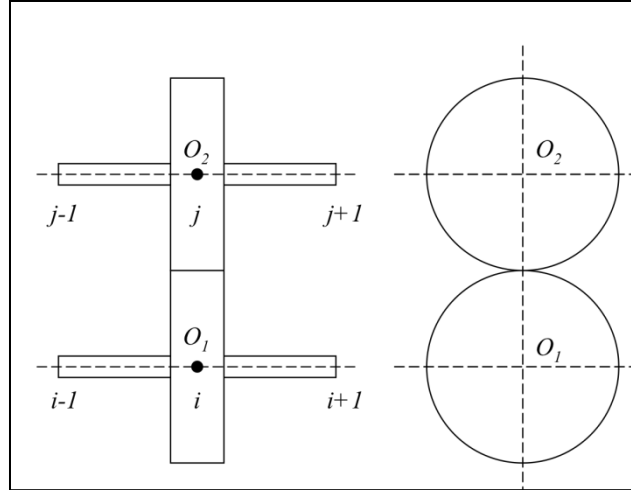


Figure 3.1.1. Gear mesh finite element representation [52]

The generalized displacements are shown in the displacement vector, labeled as \mathbf{u} , and contain those corresponding to the shaft center of one gear at node i and the other gear at node j , as indicated by the subscripts.

$$\mathbf{u} = [\mathbf{u}_i \quad \mathbf{u}_j]^T = [x_i \quad y_i \quad z_i \quad \theta_{xi} \quad \theta_{yi} \quad \theta_{zi} \quad x_j \quad y_j \quad z_j \quad \theta_{xj} \quad \theta_{yj} \quad \theta_{zj}]^T \quad (3.1.2)$$

Correspondingly, the generalized forces acting on both nodes may be represented by the external force vector, labeled as \mathbf{f} .

$$\mathbf{f} = [\mathbf{f}_i \quad \mathbf{f}_j]^T = [F_{xi} \quad F_{yi} \quad F_{zi} \quad M_{xi} \quad M_{yi} \quad M_{zi} \quad F_{xj} \quad F_{yj} \quad F_{zj} \quad M_{xj} \quad M_{yj} \quad M_{zj}]^T \quad (3.1.3)$$

These generalized forces are incorporated into the rotor dynamic model through a shift to the left-hand side of the equations of motion since the generalized forces are treated as linear with respect to the generalized displacements. This equivalent stiffness matrix,

\mathbf{K}_{mesh} , relates the generalized forces with the generalized displacements through the following matrix equation.

$$\begin{bmatrix} \mathbf{f}_i \\ \mathbf{f}_j \end{bmatrix} = -[\mathbf{K}_{mesh}] \cdot \begin{bmatrix} \mathbf{u}_i \\ \mathbf{u}_j \end{bmatrix} \quad (3.1.4)$$

3.2 Derivation of Mesh Stiffness Matrix

The element stiffness matrix \mathbf{K}_{mesh} is defined below, where K_g is the average gear mesh stiffness, and \mathbf{K}_{ii} , \mathbf{K}_{ij} , \mathbf{K}_{ji} , and \mathbf{K}_{jj} are 6x6 sub-matrices that account for the coordinate transformations from the pitch point of the gear mesh to the global coordinate system of the shaft centers. These sub-matrices will be discussed later in this section.

$$\mathbf{K}_{mesh} = K_g \begin{bmatrix} \mathbf{K}_{ii} & \mathbf{K}_{ij} \\ \mathbf{K}_{ji} & \mathbf{K}_{jj} \end{bmatrix} = K_g \begin{bmatrix} \mathbf{K}_{ii} & \mathbf{K}_{ji}^T \\ \mathbf{K}_{ji} & \mathbf{K}_{jj} \end{bmatrix} \quad (3.2.1)$$

A crucial parameter to the element stiffness matrix is the average gear mesh stiffness, K_g , which accounts for the tooth compliance. It is assumed that the stiffness of the rest of the gear body will be much more rigid than that of the teeth, which suggests that the tooth stiffness will dominate the gear dynamics. The meshing stiffness between a single pair of teeth is found either from experimental data or from previously reported analytical formulas. The analytical formula used to compute single tooth-tooth contact stiffness is provided below [31]:

$$K_g = \frac{bE_1E_2}{9(E_1 + E_2)} \quad (3.2.2)$$

where b is the tooth face width, and E_1 and E_2 are the gear and pinion elastic moduli.

The mesh stiffness formula, however, only represents the stiffness of a single pair of teeth in contact. As the gears rotate, a time varying mesh stiffness develops because the number of pairs of teeth in contact, also known as the contact ratio, alternate between one and two throughout the mesh cycle. Based on non-linear and time-varying analyses performed by D.B. Stringer [52], an average contact ratio of 1.3 was found to be a reasonable average value. The advantage of implementing an assumed constant contact ratio into the finite element model is that the solving time is greatly reduced and yet the accuracy remains reasonable. Spotts's formula for the average gear mesh stiffness may then be modified to

$$K_g = \frac{1.3bE_1E_2}{9(E_1 + E_2)} \quad (3.2.3)$$

The stiffness matrix was also generalized to account for the macro geometry of both spur and helical geared systems. These geometric parameters, which include normal pressure angle, helical angle, pitch radii, and orientation angle, are accounted for when relating the displacement of gear teeth along the line of action (LOA) to its components in the coordinate system of the shaft center [52]. The LOA is the path of force transmission between a pair of mating gears and is represented as a line that intersects with the pitch point

but is not, in general, tangent to the pitch circle. The displacements at the pitch point are resolved into the components of the shaft coordinate system through two coordinate transformations. The first transformation makes use of the normal pressure angle and helical angle to resolve components along the LOA into normal and tangential components along the pitch circle. An illustration of this transformation is provided in Figure 3.2.1 where the $X' Y' Z'$ coordinate system references components acting along or normal to the pitch circle at the pitch point. The second transformation makes use of the shaft orientation angle to relate the components along the pitch circle to those of the shaft center. Figure 3.2.2 illustrates the use of the shaft orientation angle, φ , in this transformation.

Spur geared systems require only three degrees of freedom per node because the forces and moments act solely in the plane of rotation, or in the X-Y plane in the diagram below. The displacements of interest for each gear node would be x , y , and θ_z , and therefore \mathbf{u} would consist of only six unknown displacements. That is, three displacements for the pinion and three displacements for the gear.

Helical geared systems, however, as shown in figure 3.2.1, require six degrees of freedom per node because the forces and moments now act in 3-D space and must also be functions of the helical angle, β . Therefore, \mathbf{u} must include all 12 generalized displacements if we are to include those of the gear and pinion.

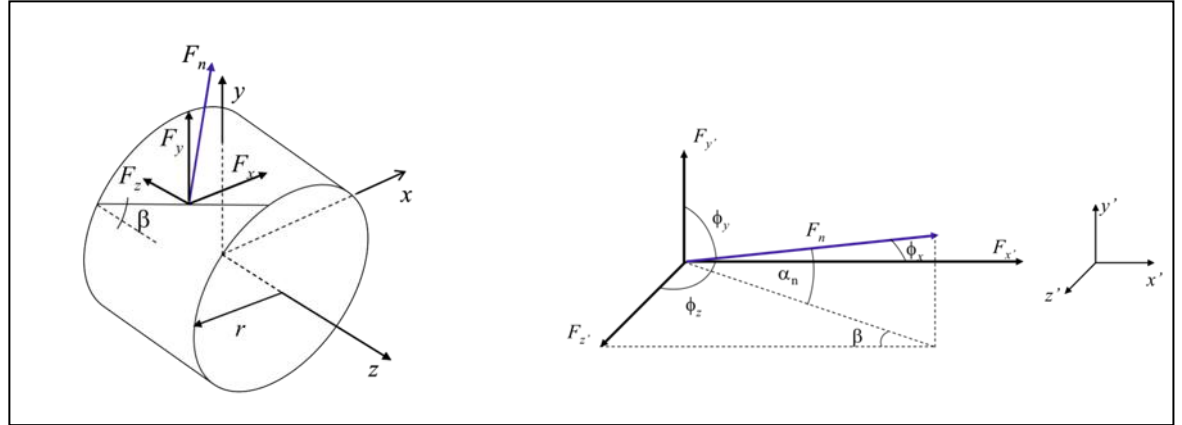


Figure 3.2.1. Gear Forces and Parameters [52]

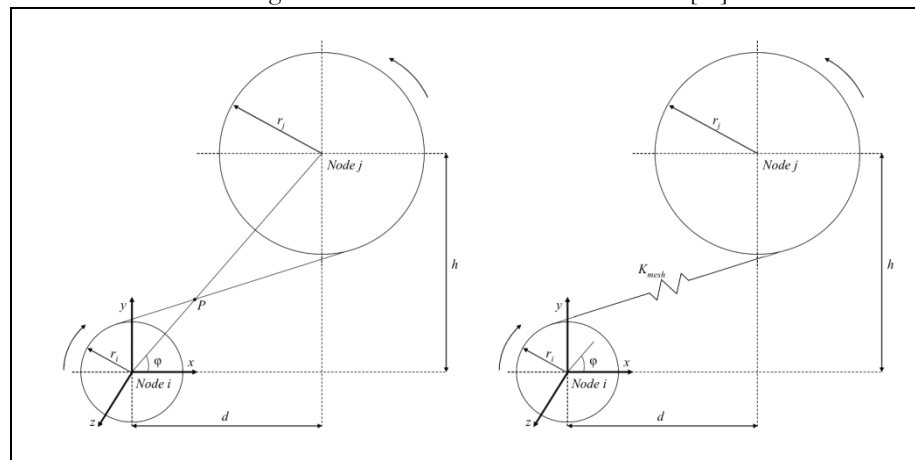


Figure 3.2.2. Gear Pair Orientation Angle [52]

The derivation of this 12x12 stiffness matrix relies on relatively few geometric inputs but is robust enough to account for parameters corresponding to those of helical and spur gear meshes. The geometric inputs for the gear and pinion include the following: pitch radii, normal pressure angle, helical angle, and an orientation angle of the shafts holding the gears. Figures 3.2.1 and 3.2.2 depict the relevant geometric parameters, and the symbols are defined in the **Nomenclature**.

The equations of motion that relate the generalized forces to the generalized displacements were obtained by applying a force balance along the LOA. The transmitted force is proportional to the net displacement of the tooth along the LOA through a

component of the mesh stiffness matrix. The transmitted force and displacement along the LOA can be resolved into components of the shaft center coordinate system through the two coordinate transformations involving the parameters mentioned above. Each element of the gear mesh stiffness matrix may then be evaluated using the Influence Coefficient method where one varies individual generalized displacements and determines the resulting generalized forces required to produce that deflection.

The direction cosines are used to resolve the transmitted force into components along the pitch circle and are convenient for notational purposes. They are functions of the helical angle and normal pressure angle as shown by the following relations:

$$\begin{aligned}\cos \phi_x &= \cos \beta \cos \alpha_n \\ \cos \phi_y &= \sin \alpha_n \\ \cos \phi_z &= \sin \beta \sin \alpha_n\end{aligned}\tag{3.2.4}$$

In summary, the resulting mesh stiffness matrix may be written as:

$$\mathbf{K}_{mesh} = K_g \begin{bmatrix} \mathbf{K}_{ii} & \mathbf{K}_{ij} \\ \mathbf{K}_{ji} & \mathbf{K}_{jj} \end{bmatrix} = K_g \begin{bmatrix} \mathbf{K}_{ii} & \mathbf{K}_{ji}^T \\ \mathbf{K}_{ji} & \mathbf{K}_{jj} \end{bmatrix}\tag{3.2.5}$$

\mathbf{K}_{ii} , \mathbf{K}_{ij} , \mathbf{K}_{ji} , and \mathbf{K}_{jj} are 6x6 sub-matrices that represent the geometric contributions of the helical angle, normal pressure angle, pitch radii, and the orientation angle of the gears to the element stiffness matrix. Those sub-matrices are expressed in Eq (3.2.6).

The previous section illustrated how to produce the 12x12 gear mesh stiffness matrix from several key parameters that included material, and geometric properties of the gears. This section will explore how one incorporates the element stiffness matrix into the global stiffness matrix of a rotor dynamic system. The example shown below for a simple geared system will indicate the proper approach and may be applied to many more complex transmission systems with multiple gear stages.

Figure 3.3.1 shows a finite element representation of two parallel shafts joined by a gear mesh and is represented as geared system 1. As indicated in the figure, the shaft system contains 3 elements and 5 node points, where nodes 2 and 4 represent the locations of the gears. In general, the number of degrees of freedom for each node may vary depending on whether the user conducts a lateral, torsional, axial, or any coupled finite element analysis.

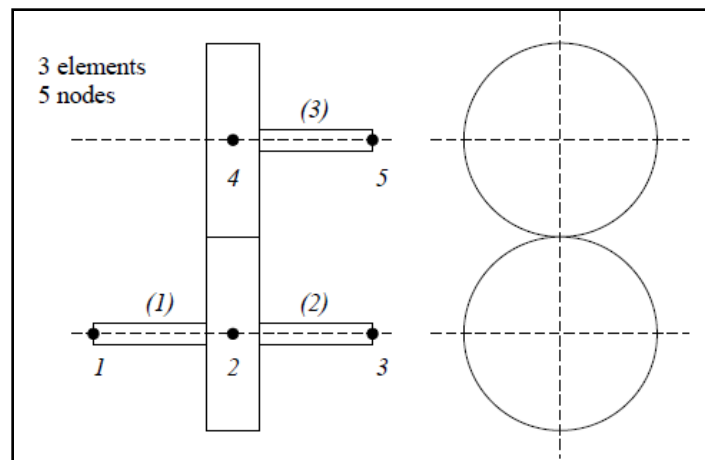


Figure 3.3.1. Finite element representation of geared system 1 [52]

To simplify the analysis and to illustrate its generality, we will express the generalized displacements of geared system 1 as the following:

$$\mathbf{u} = [\mathbf{u}_1 \quad \mathbf{u}_2 \quad \mathbf{u}_3 \quad \mathbf{u}_4 \quad \mathbf{u}_5]^T \quad (3.3.1)$$

where each \mathbf{u}_i represents all of the degrees of freedom associated with the i th node point. The global stiffness matrix may be expressed in the following way in Eq (3.3.2) without the inclusion of the mesh stiffness matrix. It is evident that there are no terms that would account for the dynamics between nodes 2 and 4.

$$[\mathbf{K}]^G \cdot \mathbf{u} = \begin{bmatrix} [\mathbf{k}_{1,1}^{(1)}] & [\mathbf{k}_{1,2}^{(1)}] & \mathbf{0} & \mathbf{0} & \mathbf{0} \\ [\mathbf{k}_{2,1}^{(1)}] & [\mathbf{k}_{2,2}^{(1)} + \mathbf{k}_{2,2}^{(2)}] & [\mathbf{k}_{2,3}^{(2)}] & \mathbf{0} & \mathbf{0} \\ \mathbf{0} & [\mathbf{k}_{3,2}^{(2)}] & [\mathbf{k}_{3,3}^{(2)} + \mathbf{k}_{3,3}^{(3)}] & [\mathbf{k}_{3,4}^{(3)}] & \mathbf{0} \\ \mathbf{0} & \mathbf{0} & [\mathbf{k}_{4,3}^{(3)}] & [\mathbf{k}_{4,4}^{(3)} + \mathbf{k}_{4,4}^{(4)}] & [\mathbf{k}_{4,5}^{(4)}] \\ \mathbf{0} & \mathbf{0} & \mathbf{0} & [\mathbf{k}_{5,4}^{(4)}] & [\mathbf{k}_{5,5}^{(4)}] \end{bmatrix} \cdot \begin{bmatrix} \mathbf{u}_1 \\ \mathbf{u}_2 \\ \mathbf{u}_3 \\ \mathbf{u}_4 \\ \mathbf{u}_5 \end{bmatrix} \quad (3.3.2)$$

The mesh stiffness matrix will provide the stiffness terms relating shared generalized forces acting on and between nodes 2 and 4, and it may be expressed in the following way.

$$[\mathbf{K}]_{\text{mesh}} \cdot \begin{bmatrix} \mathbf{u}_2 \\ \mathbf{u}_4 \end{bmatrix} = \begin{bmatrix} [\mathbf{k}_{2,2}^{\text{mesh}}] & [\mathbf{k}_{2,4}^{\text{mesh}}] \\ [\mathbf{k}_{4,2}^{\text{mesh}}] & [\mathbf{k}_{4,4}^{\text{mesh}}] \end{bmatrix} \cdot \begin{bmatrix} \mathbf{u}_2 \\ \mathbf{u}_4 \end{bmatrix} \quad (3.3.3)$$

Thus, one may reduce the 12x12 mesh stiffness matrix so that the components remaining are the ones that correspond only to the desired degrees of freedom. This provides the user with the flexibility of choosing to use the stiffness matrix to solve a lateral, axial, torsional, or a coupled rotor dynamics problem.

The final step in producing the global rotor/gear stiffness matrix is to add all of the sub-matrices of the mesh stiffness matrix corresponding to specific nodal locations to the proper locations in the global matrix. The matrix equation below illustrates this concept for geared system 1 and shows where the components of the mesh stiffness matrix were added.

$$[\mathbf{K}]^G \cdot \mathbf{u} = \begin{bmatrix} [\mathbf{k}_{1,1}^{(1)}] & [\mathbf{k}_{1,2}^{(1)}] & \mathbf{0} & \mathbf{0} & \mathbf{0} \\ [\mathbf{k}_{2,1}^{(1)}] & [\mathbf{k}_{2,2}^{(1)} + \mathbf{k}_{2,2}^{(2)}] + [\mathbf{k}_{2,2}]_{\text{mesh}} & [\mathbf{k}_{2,3}^{(2)}] & [\mathbf{k}_{2,4}]_{\text{mesh}} & \mathbf{0} \\ \mathbf{0} & [\mathbf{k}_{3,2}^{(2)}] & [\mathbf{k}_{3,3}^{(2)} + \mathbf{k}_{3,3}^{(3)}] & [\mathbf{k}_{3,4}^{(3)}] & \mathbf{0} \\ \mathbf{0} & [\mathbf{k}_{4,2}]_{\text{mesh}} & [\mathbf{k}_{4,3}^{(3)}] & [\mathbf{k}_{4,4}^{(3)} + \mathbf{k}_{4,4}^{(4)}] + [\mathbf{k}_{4,4}]_{\text{mesh}} & [\mathbf{k}_{4,5}^{(4)}] \\ \mathbf{0} & \mathbf{0} & \mathbf{0} & [\mathbf{k}_{5,4}^{(4)}] & [\mathbf{k}_{5,5}^{(4)}] \end{bmatrix} \cdot \begin{bmatrix} \mathbf{u}_1 \\ \mathbf{u}_2 \\ \mathbf{u}_3 \\ \mathbf{u}_4 \\ \mathbf{u}_5 \end{bmatrix} \quad (3.3.4)$$

The steps necessary to conduct a rotor dynamic analysis of helical and spur geared transmission systems are complete. The methods used to produce the gear mesh stiffness matrix have been illustrated in section 3.2, and the techniques for incorporating this matrix into a global finite element model have been shown in this section, 3.3. Chapters 4 and 5 will demonstrate the applicability of the gear mesh stiffness matrix within the finite element code to two different industrial geared rotor systems.

Chapter 4 Industrial Gearbox Application 1

4.1 Introduction

Chapter 3 discussed the methodology of adding gearbox dynamics to a rotor dynamic analysis and this chapter will illustrate its applicability to an industrial steam-turbine-generator set. Excess levels of rotor lateral vibration were reported in this drive-train which has a rated electrical power output of 12 MW. The train also contained a speed-reducing gearbox, and a flexible coupling in between the turbine and generator. An overall schematic of the rotating machine is shown below in Fig. 4.1.1. The steam turbine is designed to run at a nominal operating speed of 10,770 rpm. The gearbox reduces the rotational speed from 10,770 rpm to 1,500 rpm at the generator. The electrical generator is coupled to the low-speed output of the gearbox. This arrangement is suitable for the generation of electrical power at 50 Hz while allowing the turbine to operate at peak efficiency.

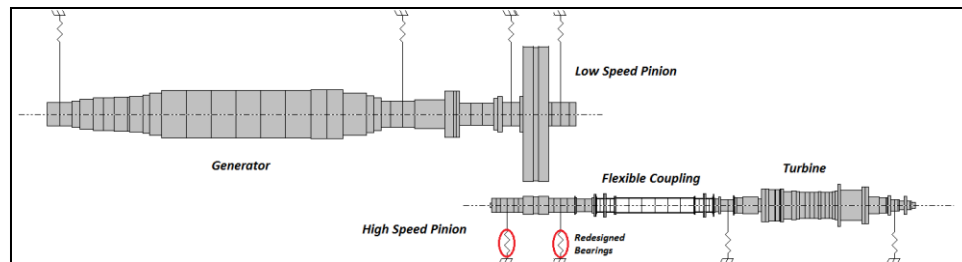


Figure 4.1.1. Overall steam-turbine generator system model.

Measurements indicated sub-synchronous vibration along the high-speed turbine /high-speed pinion shaft at 9,869 rpm during spin testing of the turbine and gearbox. This vibration increased in amplitude as the running speed was increased to 10,409 rpm. The

reported vibration had a 63 μm peak and occurred at about 0.85-0.89X, where X is the operating speed of the high-speed shaft. Since the generator was uncoupled from the turbine and gearbox during the spin testing, the gearbox bearings were lightly loaded.

A frequency spectrum plot of vibration along the high-speed shaft at a running speed of 10,201 rpm is shown below in figure 4.1.2. The synchronous vibration due to unbalance forces is approximately 35 μm , while the sub-synchronous component, at 0.85X, is 58 μm . Several spectrum plots of different running speeds were provided and illustrate the trend of increasing sub-synchronous amplitude as the running speed was increased.

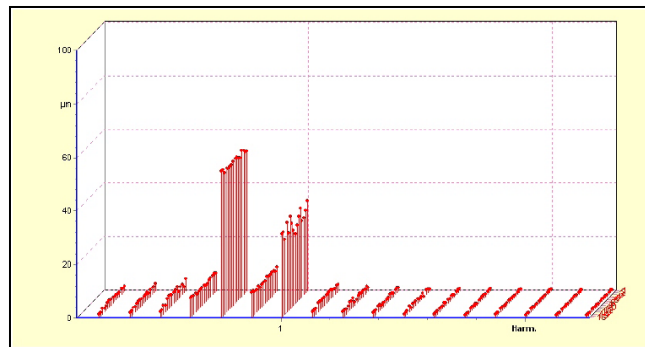


Figure 4.1.2. Spectrum plot of HS shaft at 10,201 rpm (units in μm)

Free oil was discovered in the high-speed coupling between the turbine and the generator during subsequent investigations. The turbine and gearbox were able to reach the nominal operating speed of 10,770 rpm after the excess oil had been removed. After increasing the speed of the turbine to ensure that over-speed requirements could be met, the high vibration levels were observed again. Since then, the turbine and gearbox could not exceed 7,000 rpm without tripping. Leakage from the turbine coupling side bearing was identified as the source of the excess oil in the coupling. No oil seal leakage from the gearbox was reported.

Reports in the literature suggest that trapped liquid in rotors produces sub-synchronous whirl very similar to the above observations. For a nominal deflection of the rotor, the trapped fluid experiences centrifugal forces in the radial direction. The spinning surface of the cavity combined with the finite viscosity of the fluid, however, produce tangential forces that can induce forward whirl and thus form the basis of sub-synchronous instability [43]. In 1967, Ehrich produced a simple analytical model which predicts whirl frequency and whirl amplitude as a function of supercritical rotor speed, liquid mass ratio, and a parameter related to the fluid Reynold's number and damping ratio [7]. His findings suggest that the ratio of whirl frequency to onset speed can vary from 0.5-1X depending on the mass ratio and stability characteristics.

In 1968, Wolf developed a more advanced analytical model that predicts a rotor speed region of unstable self-excited whirl as a function of liquid mass ratio, fill ratio, and rotor critical speed [8]. His analysis suggests that unstable whirl will not develop for rotor speeds less than the reduced critical or rotor speeds above $1.707 \cdot \omega_o$, where ω_o is the emptied rotor critical speed. This places the unstable whirl frequency approximately between 0.6-1X.

Ota et al. conducted several experiments that tested how changes in the properties of liquids affect the width of the unstable rotor speed region [35]. They concluded that increases in viscosity do not change the width of the unstable region, but they decrease the growth rate of instability through damping. Increases in specific gravity, however, contribute to wider and more violent unstable regions. These experiments validated the models proposed by Ehrich and Wolf.

Additional authors have observed and measured vibration resulting from trapped fluid in hollow rotors. Ehrich observed an asynchronous whirling motion induced by small amounts of free oil or condensed water in a hollow rotor of an aircraft gas turbine [7]. Kirk reported that entrained oil in the couplings of compressors has repeatedly produced sub-synchronous vibration ranging from 0.83-0.94X [24].

Subsequent rotor dynamic modeling and simulations are conducted here to verify that the entrained oil in the high-speed coupling would produce the observed sub-synchronous vibration for this steam-turbine generator.

4. 2 Gearbox Rotor Dynamic Analysis

The complete steam-turbine generator rotor dynamic system can be decomposed into subsystems, which allows various models of components to be integrated into the full system. Accurate results are obtained from performing free vibration and unbalance response analyses on this subsystem because the gearbox connections to the low-speed and high-speed shafts are flexible enough to expect vibration isolation. An analysis of the full rotor dynamic system was conducted and confirmed this assumption. This section will focus on developing a rotor dynamic model of the gearbox using Timoshenko beam elements. The beam elements are widely used to model rotors as they have been shown to produce accurate results when compared to experimental data [51]. The code performs steady-state rotor dynamic analyses and has lateral, torsional, and axial degrees of freedom. The finite element model of the gearbox is shown below in Figure 4.2.3.

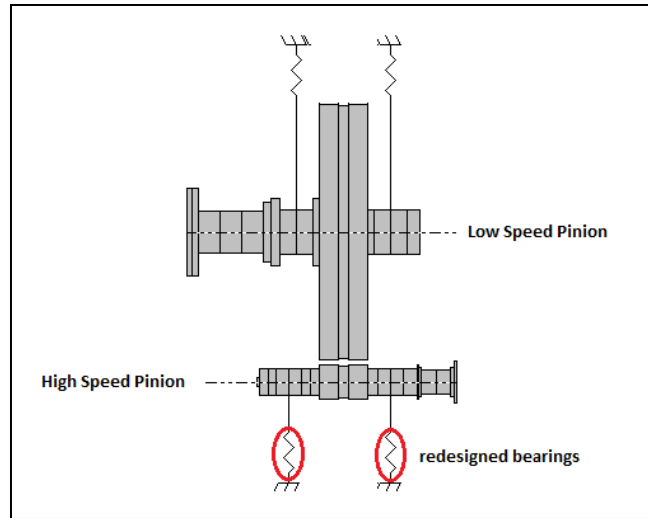


Figure 4.2.3. Gearbox finite element beam model

Stability and unbalance response analyses were completed using ten different generator load cases, which are provided in table 4.2.1, and two different sets of gearbox bearings. Each load case was run at the prescribed operating speed of 10,778 rpm. Loads 1, 5, and 10 were taken to represent a light, medium, and heavy loaded case and were examined in greater detail. The bearing load cases show the Cartesian force components in both SI and English units.

Load Case	f_x	N	f_y	N
	lb _f		lb _f	
1	0.4	2	-185.7	-826
2	22.4	100	-132.1	-588
3	223.7	995	360.9	1605
4	447.5	1991	908.8	4043
5	1119	4978	2552	11352
6	2014	8959	4743	21098
7	2909	12940	6935	30848
8	3804	16921	9126	40594
9	4699	20902	11317	50341
10	5594	24883	13508	60087

Table 4.2.1. Generator load cases

The analyses were conducted using two different sets of gearbox bearings. The original gearbox fluid film bearings were two-pad offset halves bearings and were the first to be included in the stability and unbalance response analyses. It was crucial to analyze the original bearing set to validate the accuracy of the rotor dynamic model before recommending a solution to the instability. Also, it would provide greater insight into why the gearbox high-speed shaft would experience instability under certain load cases. The redesigned bearing set consisted of three-lobe pressure dam bearings.

4.3 Stability Analysis

Rotor dynamic instability is fundamentally a free-vibration phenomenon where external fluid cross-coupled stiffness and electromagnetic negative stiffness act on the rotor. These stiffness values act on the rotor and can excite natural frequencies of vibration. In rotor dynamic models, these stiffnesses are represented as cross-coupled or negative stiffnesses. Typical sources of destabilizing stiffnesses include fluid-structure interaction in fixed pad fluid film bearings and seals, rotor internal friction, unbalanced electromagnetic pull, and other components. When a cross-coupled stiffness of 2.84×10^7 N/m was applied to the coupling hub, it produced instability in the rotor dynamic model that was consistent with the observed measurements. This seems to indicate that the entrained oil in the coupling is a potential source of the destabilizing stiffness. The oil came from leakage from the turbine inboard bearing.

The stability is determined from the natural frequencies and mode shapes of the damped free-vibration problem:

$$\mathbf{M}\ddot{\mathbf{u}} + (\mathbf{C} + \Omega\mathbf{G})\dot{\mathbf{u}} + \mathbf{K}\mathbf{u} = \mathbf{0} \quad (4.3.1)$$

where \mathbf{M} , \mathbf{C} , \mathbf{G} and \mathbf{K} are the mass, damping, gyroscopic and stiffness matrices respectively. The finite element analysis will solve for the natural frequencies, mode shapes, and will determine the stability of the mode, which will be expressed in terms of log decrement. A log decrement value greater than zero implies that the system is stable, and a value less than zero implies that is unstable. The American Petroleum Institute requires a minimum log decrement of 0.1 to allow for unmodeled effects and to provide a factor of safety [47].

Using the gear element model from Stringer [52], the specific stiffness matrix for the gearbox was developed. Table 4.3.1 shows the relevant parameters used to model the mesh stiffness of the herringbone gearbox.

Parameter	Value	Units
E_{gear}	206×10^9	Pa
E_{pinion}	206×10^9	Pa
R_{gear}	653.2	mm
R_{pinion}	90.9	mm
α_n	0.349	rad
β	0.471	rad
b	100.5	mm
φ	0	rad

Table 4.3.1 Gear box properties

Substituting the values given in Table 4.3.1 into Eq. (3.2.3) gives us the following average mesh stiffness. Note: the herringbone arrangement requires that we multiply Eq. (3.2.3) by a factor of 2.

$$K_g = 2.8357 \cdot 10^{11} \text{ N/m}$$

Substituting the values for the helix angle and normal pressure angle into Eq. (3.2.4)

gives the following direction cosines.

$$\cos \phi_x = 0.8373$$

$$\cos \phi_y = 0.3420$$

$$\cos \phi_z = 0.1553$$

The final 12x12 gear element stiffness matrix, in SI units, is then:

$$K_{mesh} \cdot \bar{Q} = \begin{bmatrix} 350 & -856 & 0 & 0 & -104 & -559 & -350 & 856 & 0 & 0 & 14.4 & 77.8 \\ -856 & 2100 & 0 & 0 & 254 & 1370 & 856 & -2100 & 0 & 0 & -35.3 & -191 \\ 0 & 0 & 0 & 0 & 0 & 0 & 0 & 0 & 0 & 0 & 0 & 0 \\ 0 & 0 & 0 & 0 & 0 & 0 & 0 & 0 & 0 & 0 & 0 & 0 \\ -104 & 254 & 0 & 0 & 30.8 & 166 & 104 & -254 & 0 & 0 & -4.28 & -23.1 \\ -559 & 1370 & 0 & 0 & 166 & 894 & 559 & -1370 & 0 & 0 & -23.1 & -124 \\ -350 & 856 & 0 & 0 & 104 & 559 & 350 & -856 & 0 & 0 & -14.4 & -77.8 \\ 856 & -2100 & 0 & 0 & -254 & -1370 & -856 & 2100 & 0 & 0 & 35.3 & 191 \\ 0 & 0 & 0 & 0 & 0 & 0 & 0 & 0 & 0 & 0 & 0 & 0 \\ 0 & 0 & 0 & 0 & 0 & 0 & 0 & 0 & 0 & 0 & 0 & 0 \\ 14.4 & -35.3 & 0 & 0 & -4.28 & -23.1 & -14.4 & 35.3 & 0 & 0 & 0.596 & 3.21 \\ 77.8 & -191 & 0 & 0 & -23.1 & -124 & -77.8 & 191 & 0 & 0 & 3.21 & 17.3 \end{bmatrix} \cdot 10^6 \begin{bmatrix} x_i \\ y_i \\ z_i \\ \theta_{xi} \\ \theta_{yi} \\ \theta_{zi} \\ x_j \\ y_j \\ z_j \\ \theta_{xj} \\ \theta_{yj} \\ \theta_{zj} \end{bmatrix}$$

Where the nodal coordinates are in the following order:

$$\begin{bmatrix} x_i & y_i & z_i & \theta_{xi} & \theta_{yi} & \theta_{zi} & x_j & y_j & z_j & \theta_{xj} & \theta_{yj} & \theta_{zj} \end{bmatrix}^T$$

The nodal coordinates z_i , θ_{xi} , z_j , and θ_{xj} are all equal to zero because the herringbone arrangement eliminates thrust loads and the horizontal alignment of the shafts prevents bending moments about the x-axis.

The stability analysis was performed for all generator load cases and for both bearing designs. The critical speeds, mode shapes, and log decrement values for the lowest and highest load cases are shown.

No Load		Max Load	
Log dec	Frequency (RPM)	Log dec	Frequency (RPM)
5.26	1318	19.80	647
4.15	1799	15.09	743
-0.12	6973	9.41	5667
0.00	12103	8.42	6794
10.33	12605	0.31	16104
0.10	17110	0.18	17202
0.19	17515	5.85	22623
3.82	26281	1.11	22629
0.87	29127	-0.27	27618
0.46	36108	0.96	28146

Table 4.3.2. Eigenvalues for original 2-lobe offset halves bearing

No Load		Max Load	
Log dec	Frequency (RPM)	Log dec	Frequency (RPM)
5.26	1318	19.79	647
4.25	1821	15.09	743
7.04	7129	10.98	7077
4.28	11542	9.56	9264
10.42	12425	0.31	16104
0.10	17104	0.18	17202
0.19	17509	5.85	22623
3.83	26343	1.11	22630
0.41	27558	-0.23	27416
1.39	28734	1.10	28150

Table 4.3.3. Eigenvalues for final 3-lobe pressure dam bearing

It is evident that the third mode from the original bearing is unstable when there is no load from the generator. However, at higher load cases, the high-speed shaft is well-damped and stable up to the operating speed. The unstable third mode from load case 1 is

illustrated in figure 4.3.1 and represents whirl. In contrast to the original bearing, the final one is expected to be well-damped for both minimum and maximum load cases up to operating speed.

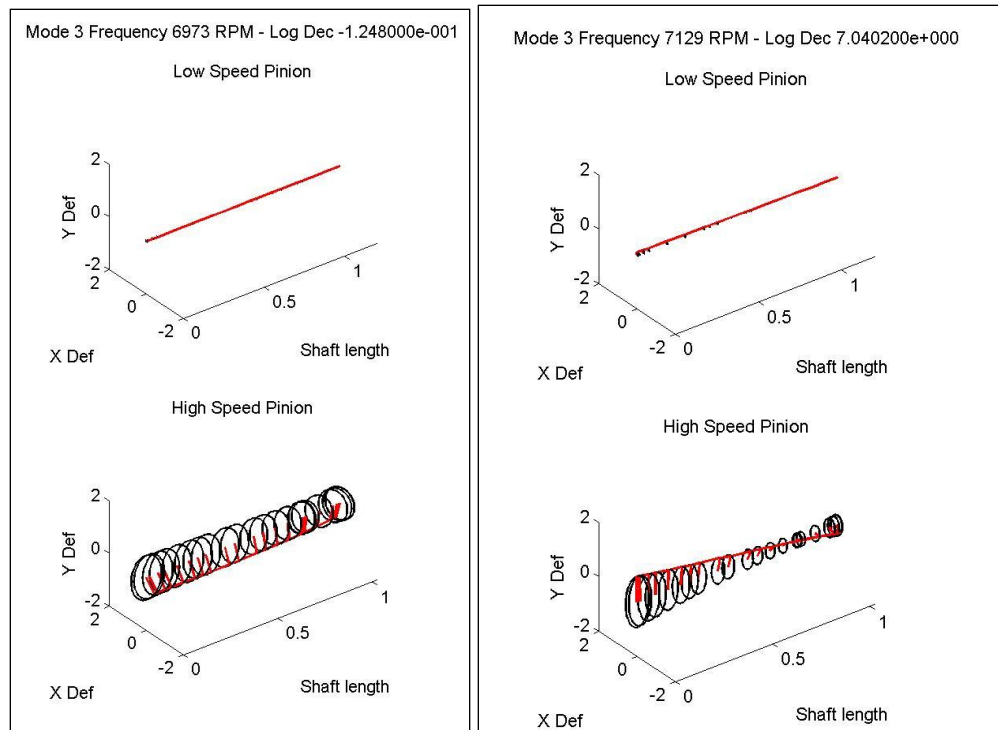


Figure 4.3.1. Eigenvalue comparison of mode 3 with original and final bearings respectively

4.4 Bearing Redesign Analysis

A three-lobed pressure dam bearing was designed as a proposed replacement for the original 2-lobe offset halves bearing. The three-lobe design with two pressure dams is based on bearing designs previously reported by Nicholas [36]. Given the load direction, a three-lobed bearing with pad parameters reported in Table 4.4.1 was deemed appropriate for the analysis:

Pad	Pivot Angle, deg	Arc Length, deg	Axial Length		Preload	Offset
			in	mm		
1	52.5	97	5.12	130	0.33	0.5
2	172.5	97	5.12	130	0.33	0.5
3	292.5	97	5.12	130	0.33	0.5

Table 4.4.1. Three Lobe Pressure Dam Pad Geometry

Pressure dams were added to the second and third pads with the following parameters:

Pad	Arc Length, deg	Axial Length		Depth
		in	mm	
1	0	0	0	0
2	60	3.54	90	0.0086
3	60	3.54	90	0.0086

Table 4.4.2. Three Lobe Pressure Dam Geometry

A shaft diameter of 5.501 in (140 mm) and radial clearance of 0.006in (152.4 μm) were used in this model. Fig. 4.4.1 gives the stiffness and damping values obtained from this new design.

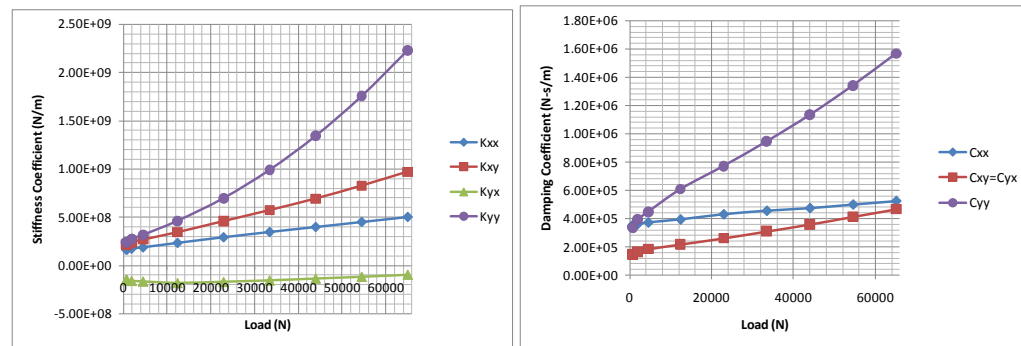


Figure 4.4.1. Stiffness and Damping Coefficients vs. Load, 3-Lobed Bearing

Using these pad and dam geometries, the pads containing the pressure dams are predicted to force the journal into a stable position for the low load cases. For the higher load cases, the pressure dams should become increasingly less influential and the load itself should force the journal to a stable position. Figure 4.4.2 illustrates the eccentricity plot for the new bearing design. The eccentricity ratios for this bearing design look very satisfying for all load cases. They range in value from 0.3305 to 0.8862; values that are generally indicative of a very stable bearing. They are not located anywhere near the center of the bearing nor do they cross the center. These results support the stability analysis that was conducted in Section 4.3.

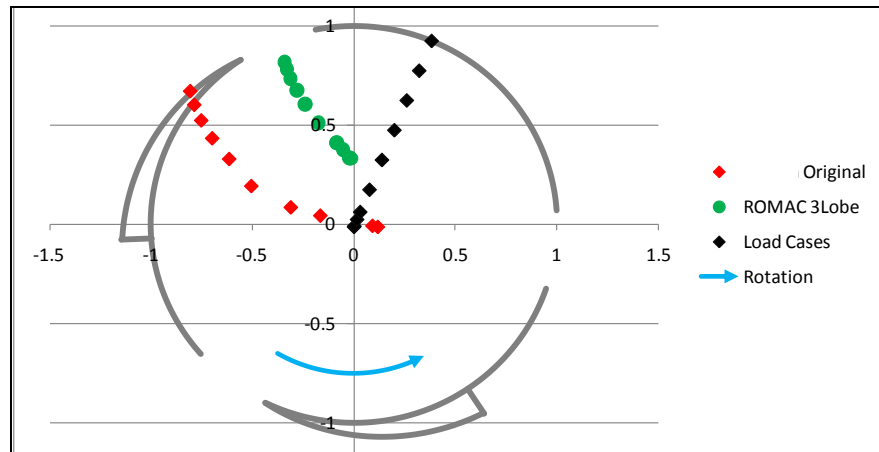


Figure 4.4.2. Eccentricity Plot- 3-Lobed Bearing

Pressure profiles over the pads of the new bearing design verify that the bearing is operating as predicted. Figure 4.4.3 illustrates pressure profiles for the first load case. As anticipated, the pads containing the pressure dams dominate the third pad in this case and force the eccentricity ratio to a safe distance from the center. The pressure dams are acting as desired for the low load cases.

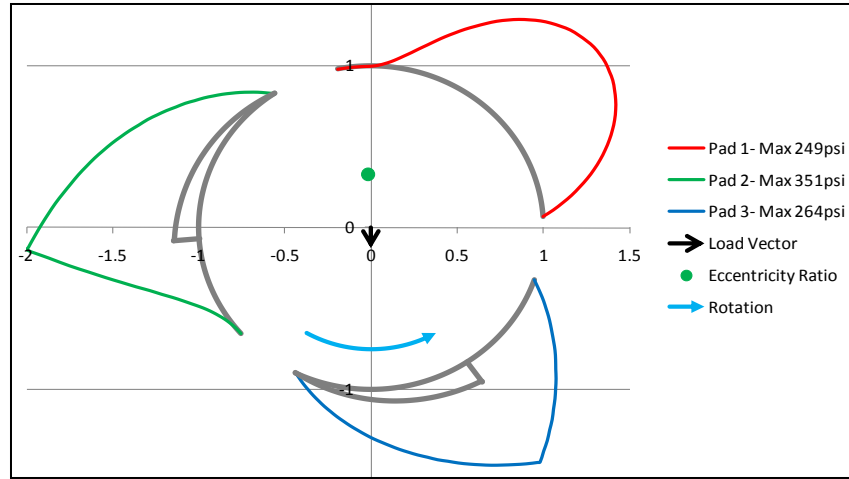


Figure 4.4.3. Pressure Profile- 3 Lobe Bearing Design, Load Case 1 $f_x = 0.4$ lbf (2 N), $f_y = -185.7$ lbf (-826 N)

Figures 4.4.4 and 4.4.5 display pressure profiles for load cases 5 and 10, respectively. As the strength of the load increases, it dictates the position of the journal. The load places increasing pressure on Pad 1 and the pressure dams become less influential. The eccentricity ratios for these cases remain in stable positions and a safe distance from the bearing wall. The three-lobed pressure dam bearing is performing as expected and appears to be a very good design for the given load conditions.

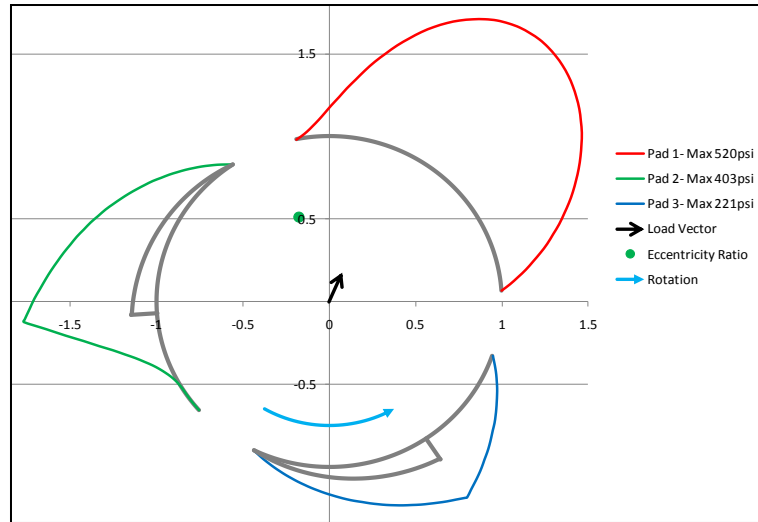


Figure 4.4.4. Pressure Profile- 3 Lobe Bearing Design, Load Case 5 $f_x = 1119$ lbf (4978 N), $f_y = 2552$ lbf (11,352 N)

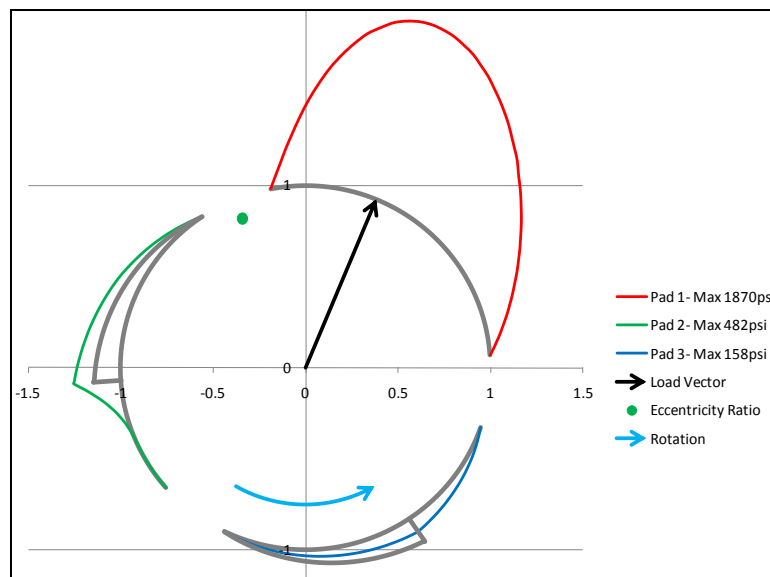


Figure 4.4.5. Pressure Profile- 3Lobe Bearing Design, Load Case 10

$f_x = 5594$ lbf (24,883 N), $f_y = 13,508$ lbf (60,087 N)

In order to assure that manufacturing tolerances would not adversely affect the performance of the bearing, a sensitivity analysis was conducted. The previous 3-lobed bearing design was taken to be the maximum clearance design. A minimum clearance design was also tested with the following changes in geometry, documented in Table 4.4.3:

	Geometry Changes				Pad Preload	Pocket Depth
	Shaft Diameter		Radial Clearance			
	in	mm	in	μm		
Minimum Clearance	5.502	139.75	0.00472	119.9	0.39	0.0071
Maximum Clearance	5.501	139.73	0.006	152.4	0.33	0.0086

Table 4.4.3. Three Lobe Pressure Dam Sensitivity Analysis

The bearing design proved to be robust as it performed very similarly in both cases. Figure 4.4.6 shows eccentricity ratios for these cases. Given the results of this analysis, the 3-lobe bearing design is a very good bearing for the steam-turbine-generator drive-train and should replace the existing 2-lobe offset halves bearings.

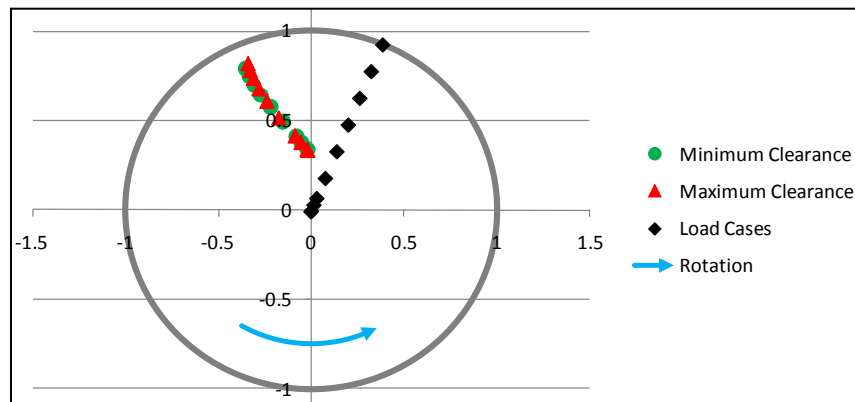


Figure 4.4.6. Eccentricity Plot- 3-Lobed Bearing, Min. and Max. Clearances

Figure 4.4.7 compares the stiffness and damping coefficients for the minimum and maximum clearance cases for the 3-lobe bearing design. The general trend for all

coefficients is nearly the same. A slight shift in magnitude can be seen; however, all values remain within the same order of magnitude and the small shift is trivial. These coefficients further illustrate the robustness of the new design. An unbalance response analysis is conducted in Section 4.5 using the final 3-lobe pressure dam bearings.

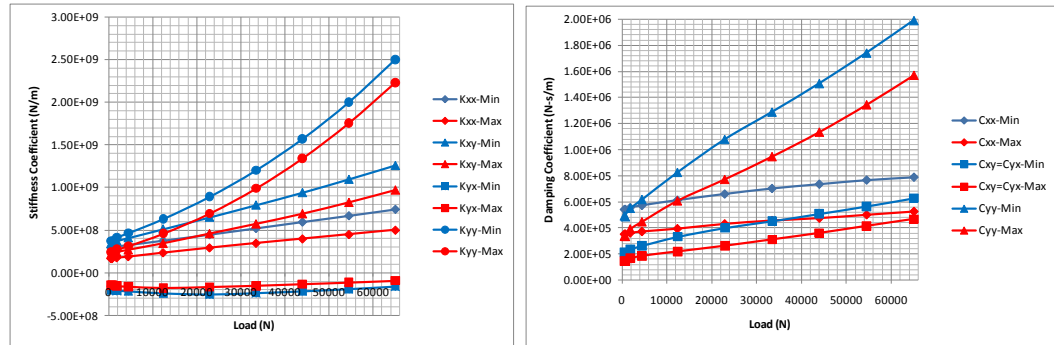


Figure 4.4.7. Stiffness and Damping Coefficients vs. Load- 3-Lobed Bearing, Min. and Max. Clearances

4.5 Unbalance Response

All rotor systems have some amount of unbalance. These small unbalances amplify the vibration of the rotor when it passes through critical modes and can have a significant impact on the behavior of the rotor system. These vibration levels, if not analyzed properly, can lead to catastrophic failure. Therefore to predict the response of the rotor system due to the unbalance, we analyze the worst case scenario and place the unbalance weights at the locations with the largest mass in the finite element model. The unbalance response was evaluated in accordance with the requirements set by API and is determined from a damped forced response analysis of the rotor model [47]. The equation for the rotor model takes the matrix form:

$$\mathbf{M}\ddot{\mathbf{u}} + (\mathbf{C} + \Omega\mathbf{G})\dot{\mathbf{u}} + \mathbf{K}\mathbf{u} = \mathbf{f} \quad (4.5.1)$$

The locations of the unbalance weights are determined based on the mode shapes for critical speeds that occur in the operating range of the rotor. The high-speed unbalance was placed at the coupling end of the HS pinion shaft. For the evaluation of the unbalance response, the maximum acceptable unbalance level is based on the following formula, as required by API [47]:

$$me_u = \frac{6350W}{N} \quad (4.5.2)$$

where W is the weight in kg and N is the operating speed in rpm. During the design phase, the amount of unbalance applied to the rotor in the analysis is required to be four times the amount specified in Eq. (4.5.2) to provide a factor of safety. The probes are placed at the bearing locations of the HS pinion shaft. The analysis was performed on 3 load cases (no-load, load case 5, max load) to give a range of the response across the load range for the final 3-lobe pressure dam bearings. The response plots and phase plots were produced for each load case using minimum and maximum bearing clearances.

The unbalance response shows that the peak response around the operating range even at the worst condition is less than 4 microns and under all conditions the amplification factor is below 2.5. The only mode that was excited was the high frequency coupling bending mode around 28,000 rpm. This mode is well above the operating range and thus can be ignored.

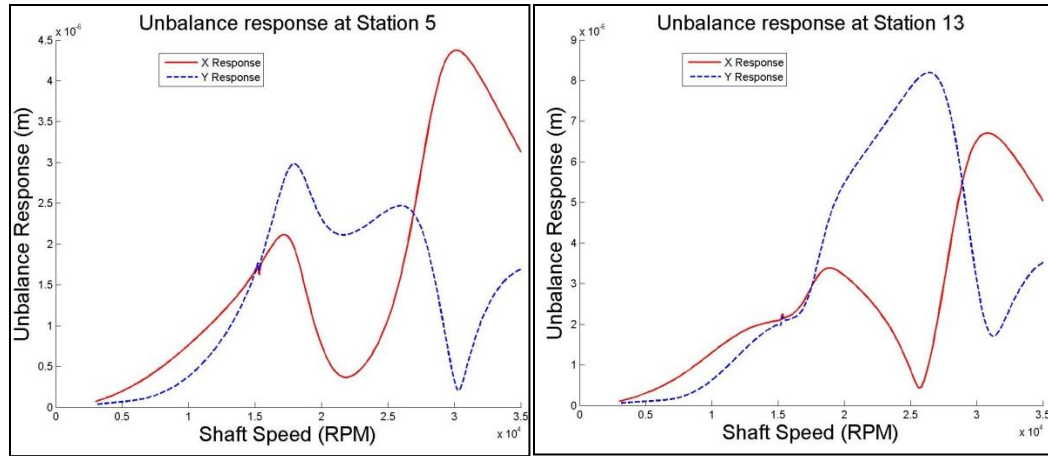


Figure 4.5.1: Response at HS pinion bearings 1, 2 – no load case – minimum clearance

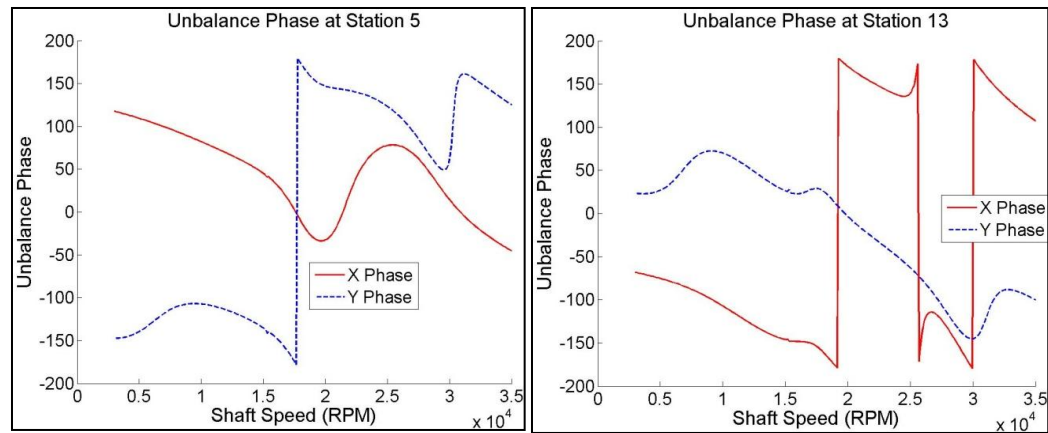


Figure 4.5.2: Phase at HS pinion bearing 1, 2 - no load – minimum clearance

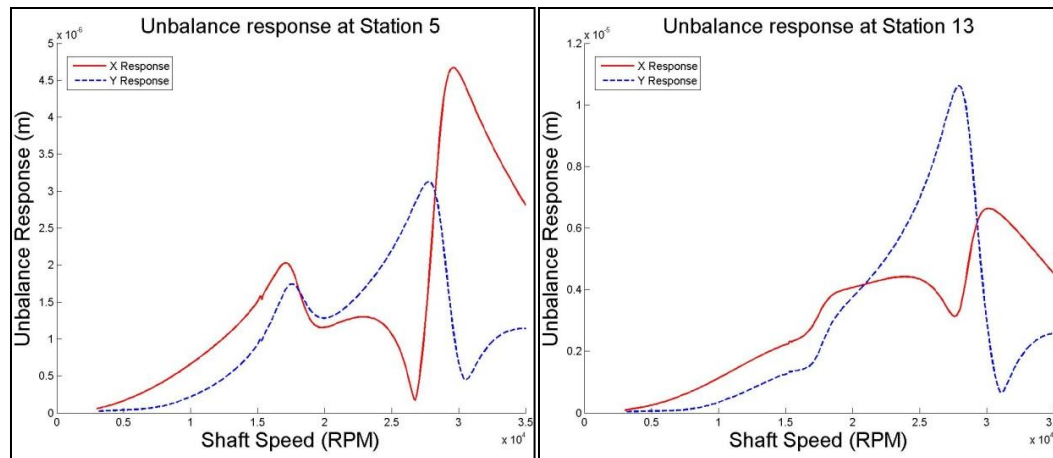


Figure 4.5.3: Response at HS pinion bearings 1, 2 – load case 5 – minimum clearance

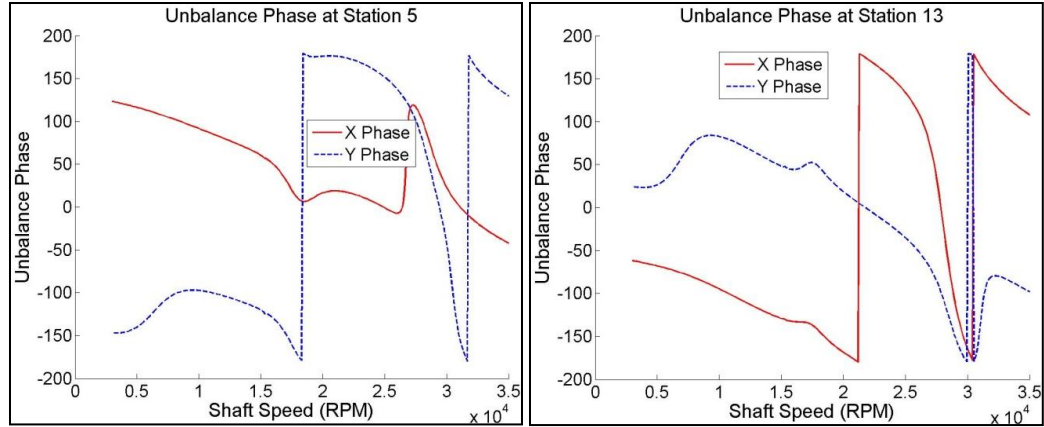


Figure 4.5.4: Phase at HS pinion bearing 1, 2 – load case 5 – minimum clearance

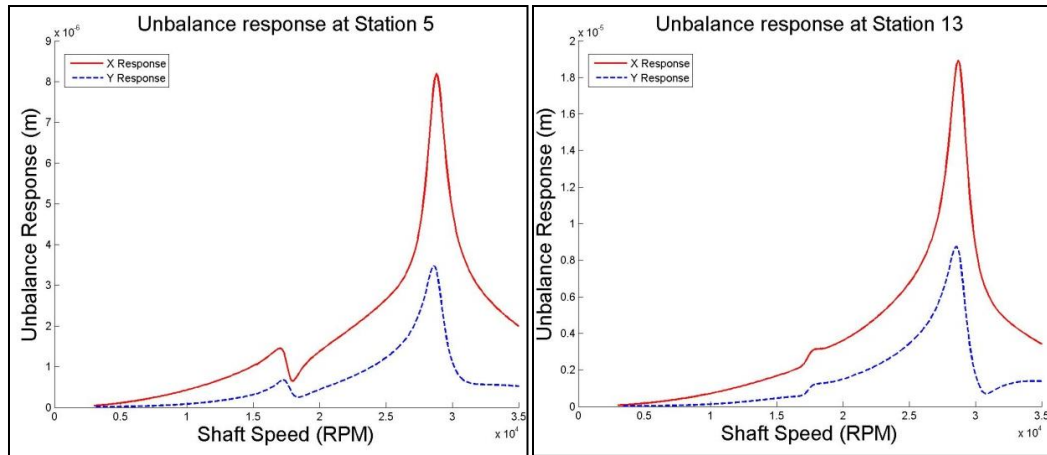


Figure 4.5.5: Response at HS pinion bearings 1, 2 – max load case 10 – minimum clearance

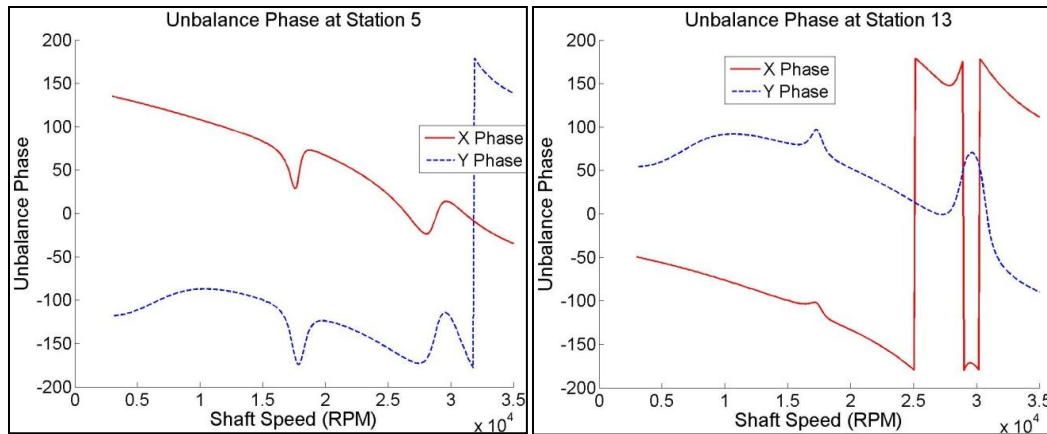


Figure 4.5.6: Phase at HS pinion bearing 1, 2 – max load case 10 – minimum clearance

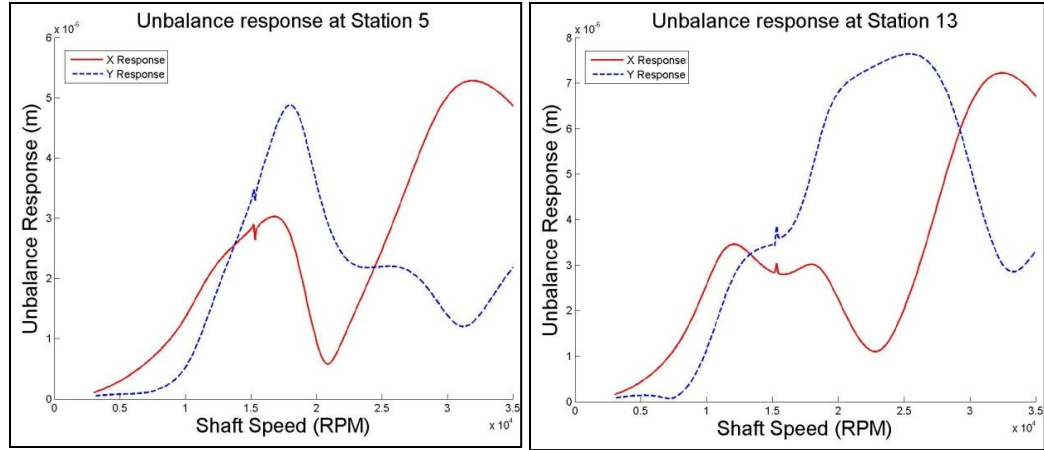


Figure 4.5.7: Response at HS pinion bearings 1, 2 – no load case 1 – maximum clearance

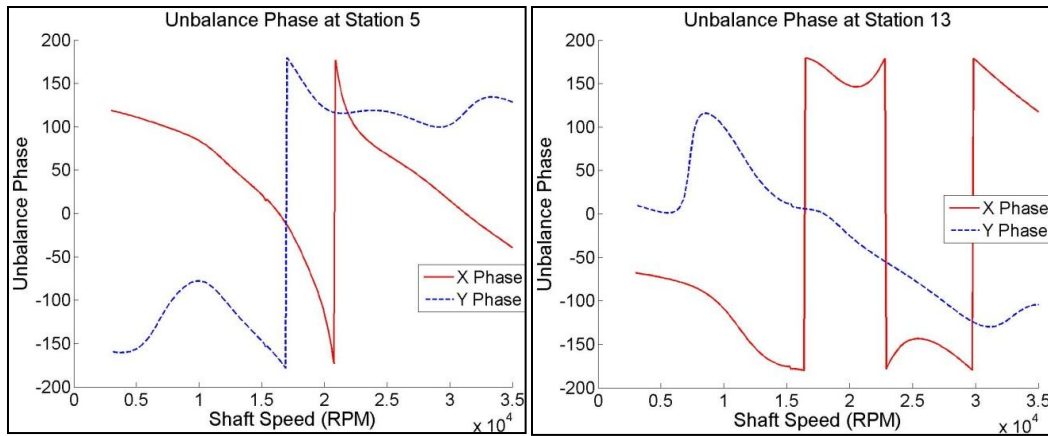


Figure 4.5.8: Phase at HS pinion bearing 1, 2, no load case 1 – maximum clearance

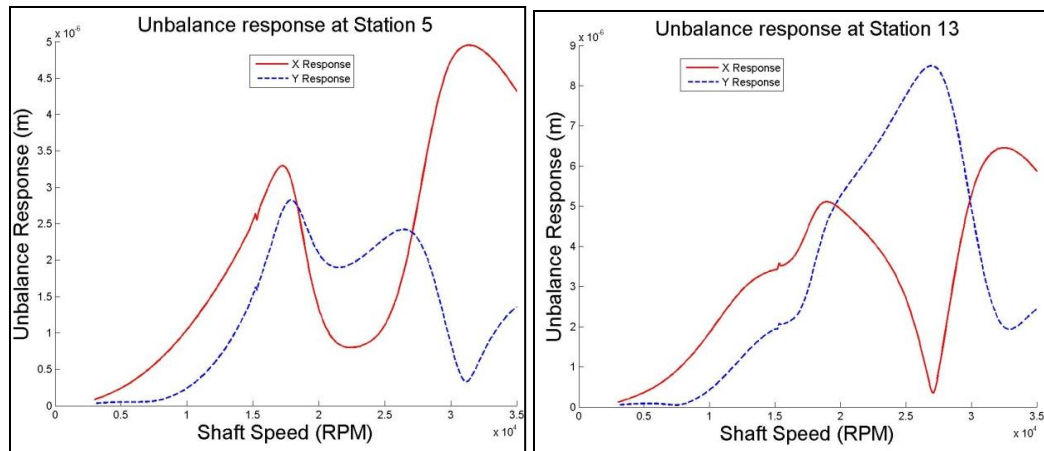


Figure 4.5.9: Response at HS pinion bearing 1, 2, load case 5 – maximum clearance

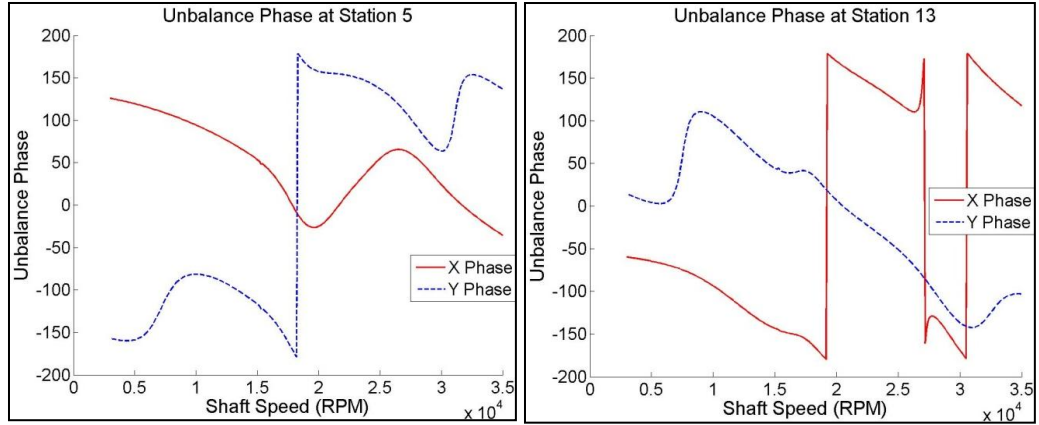


Figure 4.5.10: Phase at HS pinion bearing 1, 2, load case 5 – maximum clearance

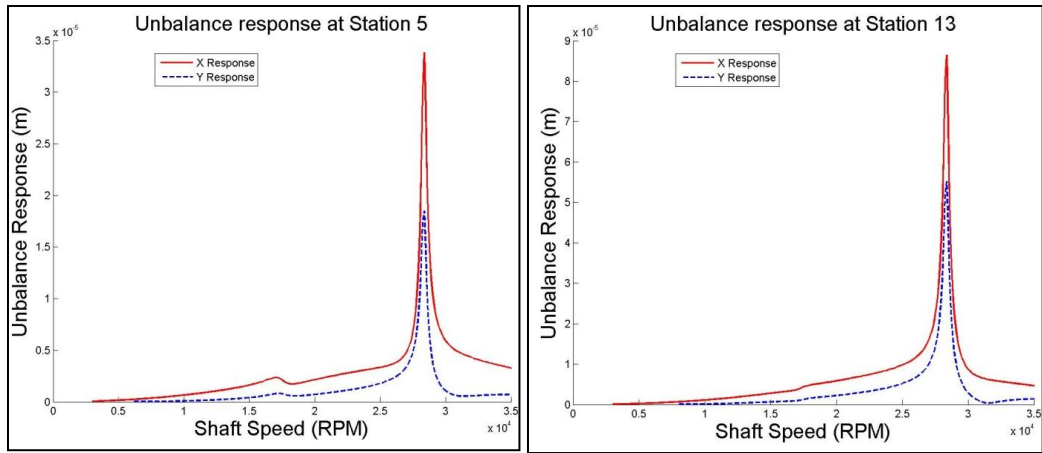


Figure 4.5.11: Response at HS pinion bearing 1, 2, max load case 10 – maximum clearance

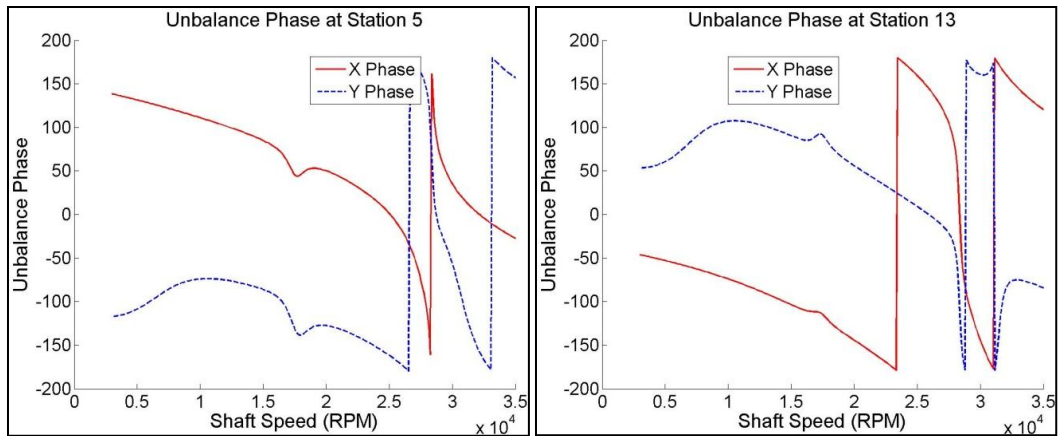


Figure 4.5.12: Phase at HS pinion bearing 1, 2, max load case 10 – maximum clearance

4.6 Conclusion

The gearbox of the steam-turbine-generator set exhibited high lateral vibration in the high-speed pinion consistent with a sub-synchronous instability at 0.86-0.89X, where X is the running speed of the high-speed pinion. The instability was shown by analysis to be a rigid-body conical whirl mode. The instability occurred when the gearbox bearings were lightly loaded as the generator was decoupled for spin testing of the turbine.

It was discovered that an oil leakage occurred from the turbine inboard bearing housing, and the oil became entrained in the high-speed coupling. Assuming that the entrained oil would produce destabilizing forces, the effects were modeled as a cross-coupled stiffness and were applied to the coupling. The instability was successfully reproduced in the model when the original bearings were lightly loaded and produced a log decrement of -0.96 and a whirl frequency ratio of 0.89X.

The conical whirl instability predicted at 0.89X is at an unusually high sub-synchronous frequency. Most whirl instability phenomena occur at frequencies of 0.3X to 0.6X. However, the analysis was able to reproduce the observed sub-synchronous frequency with low levels of cross-coupled stiffness applied to the flexible coupling. A 3-lobe bearing with two pressure dams on two of the pads was predicted to stabilize the gearbox high-speed pinion over the full range of generator load cases. Since replacing the existing bearings with the 3-lobe ones, the instability has vanished. These results validate the accuracy of the methods used to model not only the rotors and bearings but the gearbox dynamics too.

Chapter 5 Industrial Gearbox Application 2

5.1 Introduction

The second industrial gearbox application is for predicting the axial vibration of a motor-compressor drive-train, labeled as drive-train 2, before its construction. Drive-train 2 consists of a synchronous motor, low-speed flexible coupling, gearbox, high-speed flexible coupling, and a compressor as shown in figure 5.1.1. The operating speed of the motor shaft is 1,800 RPM, while the compressor shaft rotates at 4,329 RPM from the output of the speed-increasing gearbox. The gearbox arrangement is double-helical (herringbone) which offers the advantage of canceling thrust loads although they are difficult and expensive to manufacture.

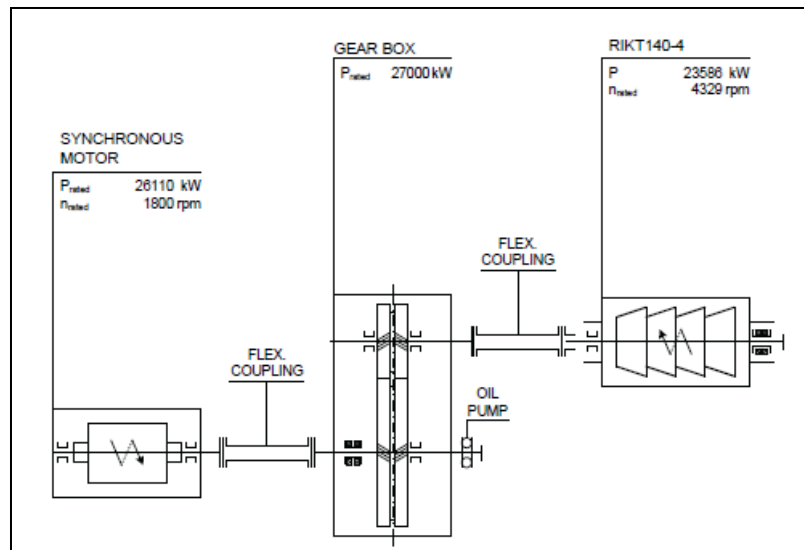


Figure 5.1.1. Drive-train 2 schematic

An undamped torsional vibration analysis has been provided by the owner of the gearbox for drive-train 2, and it illustrates twist mode shapes and their natural frequencies. These results, however, do not account for the coupling of lateral, torsional, and axial degrees of freedom produced by the dynamics inherent in helical gearboxes as are included in this thesis.

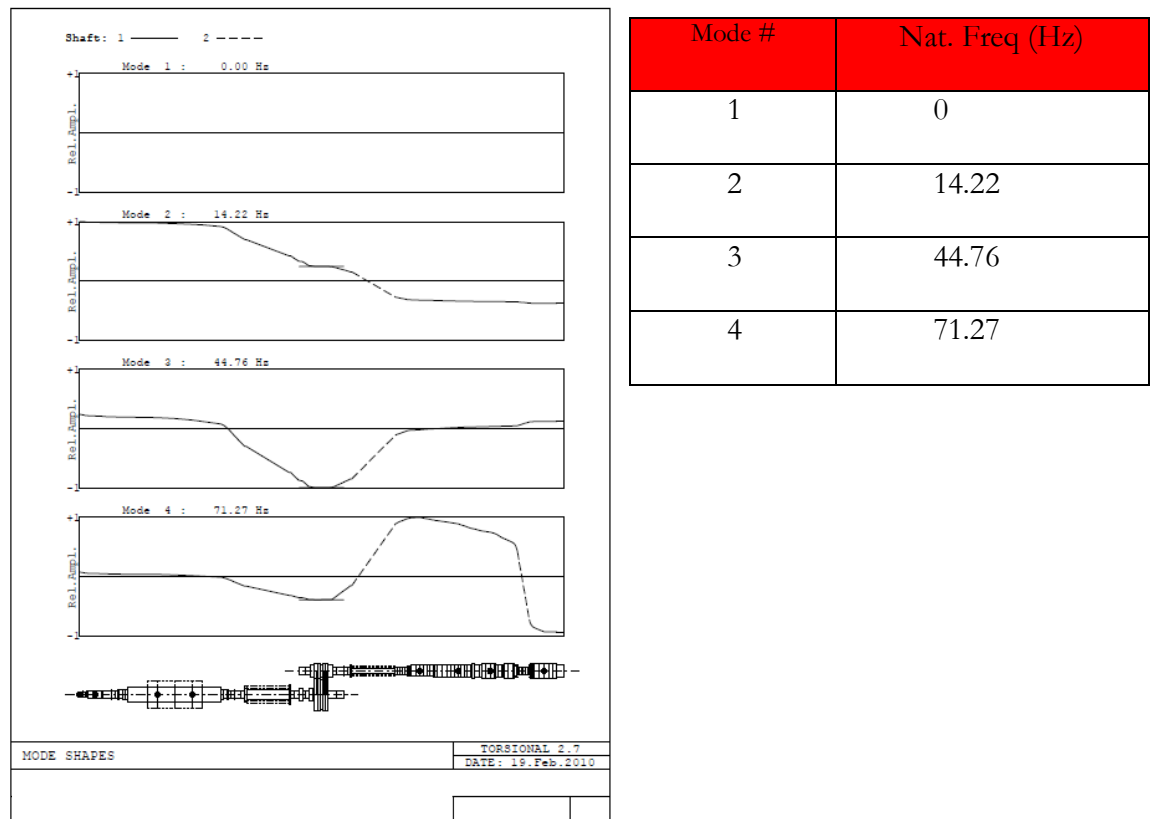


Figure 5.1.2. Calculated torsional mode shapes

No axial vibration analysis was conducted on drive-train 2 to assess whether its natural frequencies and axial modes will be excited and whether they are stable. For a similar drive-train installed in 2007, axial vibration was observed on the motor shaft with an amplitude and frequency of 2 mm and 2.8 Hz respectively. In addition, company reports

indicated that the gearbox was running noisy. An axial analysis that can predict these resonances will be mandatory for reliability considerations.

5.2 Full Shaft Finite Element Model of Drive-train 2

The rotor dynamic model for drive-train 2, which consists of a low-speed and high-speed shaft, as shown in figure 5.2.1, is split into 4 rotors in the model because the flexible couplings and the gearbox act as connectors. The first rotor consists of the synchronous motor shaft up to the low-speed coupling, and the second is the bull gear shaft. The low-speed coupling will be treated as a connector, with stiffness and damping properties, between the synchronous motor shaft and the shaft holding the bull gear. The discretization of the shafts in this model is very similar to the one provided in an undamped torsional analysis. Therefore, figures 5.2.1 through 5.2.3 apply to both the undamped torsional model and this damped coupled model.

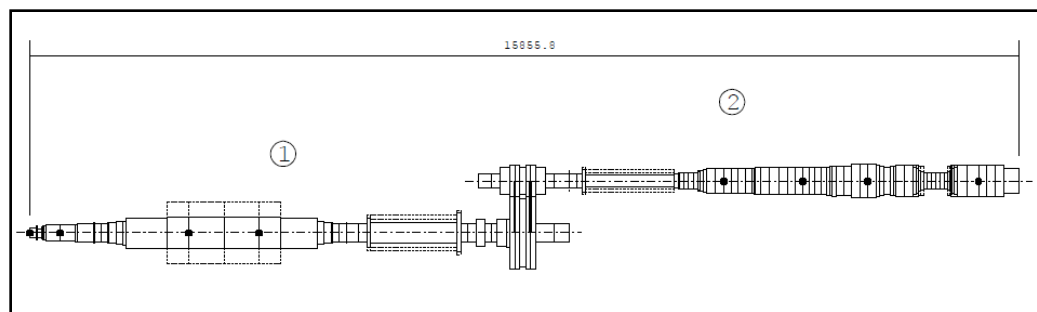


Figure 5.2.1. Discretization of the undamped torsional model of drive train 2. Similar discretizations were made in this damped coupled model.

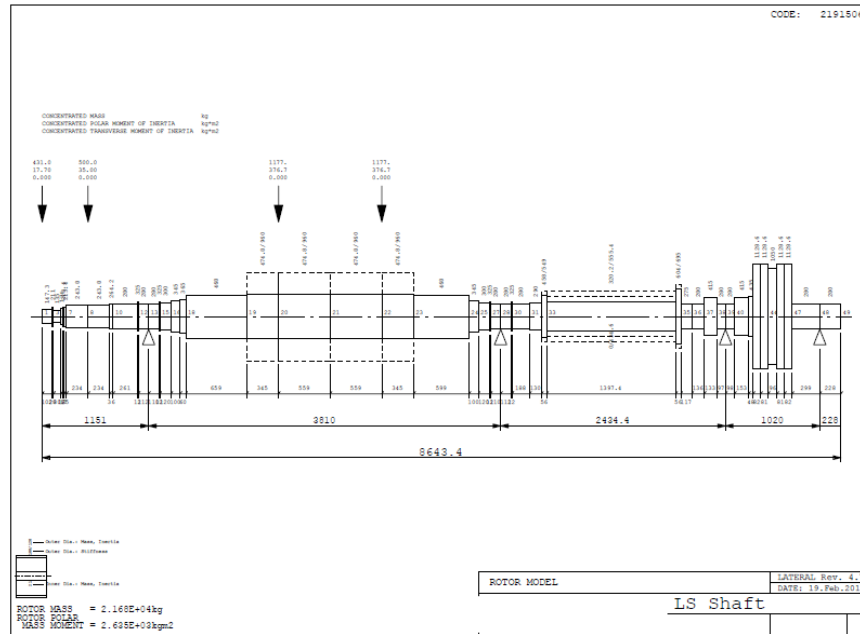


Figure 5.2.2. Drive-train 2 low-speed shaft, which corresponds to rotors 1 and 2 in the model, rotating at 1,800 RPM.

The third and fourth rotors of this drive-train 2 rotor model consist of the pinion shaft and the compressor shaft respectively. The high-speed coupling will be treated as a connector between these two shafts and will have stiffness and damping properties. Again, the finite element discretization of these shafts will be similar to what was provided for the undamped torsional analysis. Figure 5.2.3 shows the pinion shaft and compressor shaft and they represent the high-speed part of drive-train 2 rotating at 4,329 RPM.

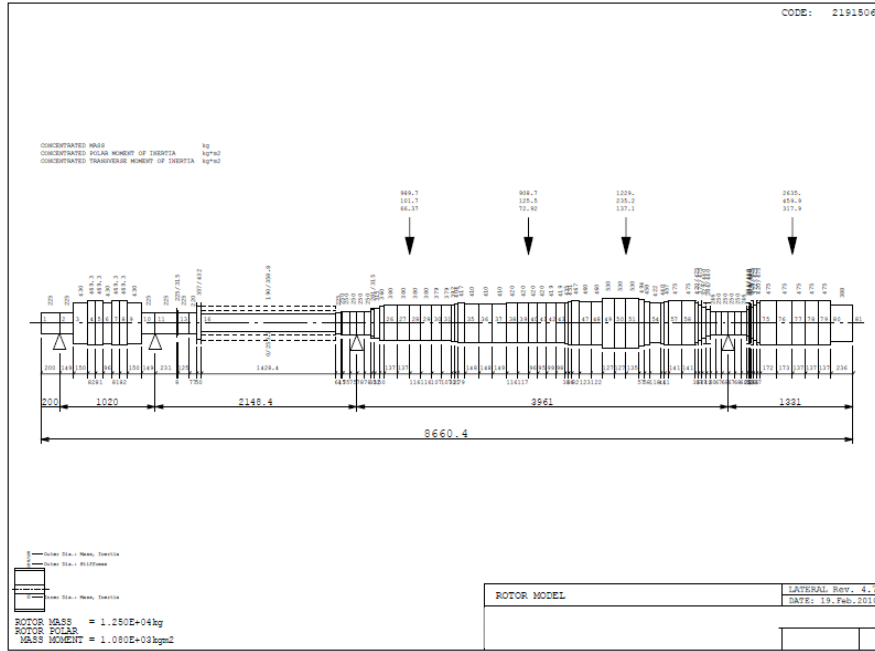


Figure 5.2.3. Drive-train 2 high-speed shaft, which corresponds to rotors 3 and 4 in the model, rotating at 4,329 RPM.

Tables 5.2.1 through 5.2.4 summarize the shaft properties and those of the external rigid masses for all 4 shafts of the drive-train 2 model. The bearings, gears, and couplings are color-coded as green, orange, and blue in tables 5.2.1 through 5.2.4 respectively, and their node numbers on each shaft are shown. The material properties used in modeling the shafts are those of structural steel.

Node #	Length (in)	OD Mass (in)	OD Stiff (in)	Mass (lbm)	Lumped Pol Iner (lbm-in ²)	Lumped Trans Iner (lbm-in ²)
1	4.02	5.80	5.80	950.18	60482.9252	39313.90138
2	0.79	8.31	8.31	0.00	0	0
3	3.15	5.31	5.31	0.00	0	0
4	0.71	6.85	6.85	0.00	0	0
5	0.67	8.40	8.40	0.00	0	0
6	0.98	8.40	8.40	0.00	0	0
7	9.21	9.60	9.60	0.00	0	0

8	9.21	9.60	9.60	1102.29	119599.0046	77739.35301
9	1.42	10.40	10.40	0.00	0	0
10	10.28	11.02	11.02	0.00	0	0
11	0.47	12.80	12.80	0.00	0	0
12	4.41	11.02	11.02	0.00	0	0
13 (brg)	4.33	11.02	11.02	0.00	0	0
14	0.47	12.80	12.80	0.00	0	0
15	4.72	11.81	11.81	0.00	0	0
16	3.94	13.58	13.58	0.00	0	0
17	2.36	14.37	14.37	0.00	0	0
18	25.94	18.43	18.43	0.00	0	0
19	13.58	37.80	18.69	0.00	0	0
20	22.01	37.80	18.69	2594.80	1287227.001	836697.5508
21	22.01	37.80	18.69	0.00	0	0
22	13.58	37.80	18.69	2594.80	1287227.001	836697.5508
23	23.58	18.43	18.43	0.00	0	0
24	3.94	13.58	13.58	0.00	0	0
25	4.72	11.81	11.81	0.00	0	0
26	0.47	12.80	12.80	0.00	0	0
27	4.33	11.02	11.02	0.00	0	0
28 (brg)	4.41	11.02	11.02	0.00	0	0
29	0.47	12.80	12.80	0.00	0	0
30	7.40	11.02	11.02	0.00	0	0
31	5.12	11.42	11.42	0.00	0	0
32	2.20	21.61	18.03	0.00	0	0
33 (cplg)	0.00	21.61	18.03	1136.47	109518.7975	71187.22

Table 5.2.1 Shaft and Mass properties of Rotor 1

Node #	Length (in)	OD Mass (in)	OD Stiff (in)	Mass (lbm)	Lumped Pol Iner (lbm-in ²)	Lumped Trans Iner (lbm-in ²)
1 (cplg)	2.20	27.36	23.78	1136.47	109518.7975	71187.22
2	4.61	10.83	10.83	0.00	0	0
3	5.35	11.02	11.02	0.00	0	0
4	5.24	16.34	16.34	0.00	0	0
5	3.82	11.02	11.02	0.00	0	0
6 (brg)	3.86	11.02	11.02	0.00	0	0
7	6.02	16.34	16.34	0.00	0	0

8	1.89	17.13	17.13	0.00	0	0
9(gear)	16.61	17.13	17.13	9277	1776904	1000000
10	11.77	11.02	11.02	0.00	0	0
11(brg)	8.98	11.02	11.02	0.00	0	0
12	0.00	11.02	11.02	0.00	0	0

Table 5.2.2. Shaft and Mass properties of Rotor 2

Node #	Length (in)	OD Mass (in)	OD Stiff (in)	Lumped Mass (lbm)	Lumped Pol Iner (lbm-in ²)	Lumped Trans Iner (lbm-in ²)
1	7.87	8.86	8.86	0.00	0	0
2 (brg)	5.87	8.86	8.86	0.00	0	0
3	5.91	16.93	16.93	0.00	0	0
4 (gear)	16.61	16.93	16.93	2747	88330	50000
5	5.91	16.93	16.93	0.00	0	0
6	5.87	8.86	8.86	0.00	0	0
7 (brg)	9.09	8.86	8.86	0.00	0	0
8	0.31	12.40	8.86	0.00	0	0
9	4.92	8.86	8.86	0.00	0	0
10	3.03	8.66	8.66	0.00	0	0
11	1.97	17.01	14.06	0.00	0	0
12(cplg)	0.00	17.01	14.06	518.08	22382	15000

Table 5.2.3. Shaft and Mass properties of Rotor 3

Node #	Length (in)	OD Mass (in)	OD Stiff (in)	Lumped Mass (lbm)	Lumped Pol Iner (lbm-in ²)	Lumped Trans Iner (lbm-in ²)
1 (cplg)	2.52	8.86	8.86	518.08	22382	15000
2	0.59	9.84	9.84	0.00	0	0
3	2.95	9.84	9.84	0.00	0	0
4	2.95	9.84	9.84	0.00	0	0
5 (brg)	3.07	9.84	9.84	0.00	0	0
6	3.07	9.84	9.84	0.00	0	0
7	1.30	12.40	11.06	0.00	0	0
8	2.05	12.40	12.40	0.00	0	0
9	1.97	14.17	14.17	0.00	0	0
10	5.39	14.96	14.96	0.00	0	0
11	5.39	14.96	14.96	0.00	0	0
12	4.57	14.96	14.96	2181.77	347452.194	226793.8839
13	4.57	14.96	14.96	0.00	0	0
14	4.21	14.92	14.92	0.00	0	0
15	4.21	14.92	14.92	0.00	0	0

16	1.26	15.43	15.43	0.00	0	0
17	1.22	15.91	15.91	0.00	0	0
18	3.11	16.42	16.42	0.00	0	0
19	5.83	16.14	16.14	0.00	0	0
20	5.83	16.14	16.14	0.00	0	0
21	5.87	16.14	16.14	0.00	0	0
22	4.57	16.54	16.54	0.00	0	0
23	4.61	16.54	16.54	0.00	0	0
24	3.78	16.54	16.54	2003.31	428916.2017	249175.9834
25	3.74	16.54	16.54	0.00	0	0
26	3.90	16.50	16.50	0.00	0	0
27	3.86	16.50	16.50	0.00	0	0
28	1.42	17.13	17.13	0.00	0	0
29	1.42	17.76	17.76	0.00	0	0
30	3.23	18.39	18.39	0.00	0	0
31	4.84	18.11	18.11	0.00	0	0
32	4.80	18.11	18.11	0.00	0	0
33	5.00	20.87	20.87	0.00	0	0
34	5.00	20.87	20.87	0.00	0	0
35	5.31	20.87	20.87	2709.77	803773.6534	468452.2156
36	2.24	19.45	19.45	0.00	0	0
37	2.28	18.03	18.03	0.00	0	0
38	4.65	16.61	16.61	0.00	0	0
39	1.61	17.32	17.32	0.00	0	0
40	1.61	17.99	17.99	0.00	0	0
41	5.55	18.70	18.70	0.00	0	0
42	5.55	18.70	18.70	0.00	0	0
43	1.42	18.70	16.54	0.00	0	0
44	1.46	18.70	14.65	0.00	0	0
45	1.85	17.32	12.95	0.00	0	0
46	1.65	17.32	11.18	0.00	0	0
47	2.36	9.69	9.69	0.00	0	0
48	2.64	9.84	9.84	0.00	0	0
49	2.68	9.84	9.84	0.00	0	0
50(brg)	2.64	9.84	9.84	0.00	0	0
51	2.68	9.84	9.84	0.00	0	0
52	2.36	9.69	9.69	0.00	0	0
53	1.10	17.32	11.18	0.00	0	0
54	0.20	17.32	11.18	0.00	0	0
55	0.47	17.32	12.95	0.00	0	0
56	1.02	18.70	12.95	0.00	0	0

57	1.42	18.70	14.65	0.00	0	0
58	1.46	18.70	16.54	0.00	0	0
59	6.77	18.70	18.70	0.00	0	0
60	6.81	18.70	18.70	0.00	0	0
61	5.39	18.70	18.70	5809.08	1571394.236	1086437.358
62	5.39	18.70	18.70	0.00	0	0
63	5.39	18.70	18.70	0.00	0	0
64	9.29	15.28	15.28	0.00	0	0
65	0.00	15.28	15.28	0.00	0	0

Table 5.2.4. Shaft and Mass properties of Rotor 4

The shafts and added-on masses are now included in the drive-train 2 model. The next sections, 5.3 through 5.5, will focus on the modeling of the bearings, couplings, and gears.

5.3 Bearings

Drive-train 2 has 7 radial bearings, and one combination radial/thrust bearing on the non-drive-end of the compressor (Rotor 4 node 50). Reasonable values of lateral stiffness and damping coefficients for all 8 bearings were assumed to be the following:

$$K_{xx} = K_{yy} = 1e6 \text{ lbf/in}$$

$$C_{xx} = C_{yy} = 100 \text{ lbf-s/in}$$

The combination radial/thrust bearing would require axial stiffness and damping coefficients. Using a separate finite element analysis for thrust bearings, values of axial stiffness and damping for this bearing were calculated to be

$$K_{zz} = 3e8 \text{ lbf/in} \quad C_{zz} = 1e6 \text{ lbf-s/in}$$

5.4 Flexible Couplings

Drive-train 2 consists of 2 flexible couplings, low-speed and high-speed, linking the motor and compressor shafts to the gear and pinion shafts respectively. Axial, lateral, and torsional stiffness and damping coefficients for each coupling are required to perform this analysis. The axial and torsional stiffness coefficients for both couplings were provided from the undamped torsional analysis and are shown below:

$$\begin{aligned} K_{0z0z \text{ LS}} &= 5.20e8 \text{ lbf-in/rad} & K_{zz \text{ LS}} &= 9.71e3 \text{ lbf/in} \\ K_{0z0z \text{ HS}} &= 6.30e7 \text{ lbf-in/rad} & K_{zz \text{ HS}} &= 1.37e4 \text{ lbf/in} \end{aligned}$$

The lateral stiffness coefficients for the flexible couplings were assumed to be very small compared to those of the bearings and thus they will have negligible influence in transmitting lateral vibrations between shafts.

Coupling damping coefficients in the lateral and torsional directions were assumed to be very small compared to those in the axial direction. The axial damping coefficients used for the flexible couplings are shown below:

$$C_{zz \text{ LS}} = C_{zz \text{ HS}} = 1e4 \text{ lbf-s/in}$$

5.5 Gearbox

The parameters required to model the gearbox stiffness coefficients include the normal pressure angle, helical angle, shaft orientation angle, pitch radii, face width, and teeth elastic moduli. The following are provided from the undamped torsional analysis:

Normal Pressure angle= α_n = 22.13 degrees

Helical angle= β =26.5 degrees

Orientation angle= φ =0 degrees

Bull Gear Pitch Radius= r_g = 22.22 inches

Pinion Pitch Radius= r_p = 9.24 inches

Face width= b =12.83 inches

Elastic Moduli= E =30e6 psi

Note: Since the gearbox has a double helical (or herringbone) arrangement, the average gear mesh stiffness was multiplied by a factor of 2.

Using the mass, stiffness, damping, and gyroscopic properties for the shafts, added-on masses, bearings, flexible couplings, and gearbox, the geared finite element analysis can assemble the global mass, stiffness, damping, and gyroscopic matrices with 6 degrees-of-freedom at each node. The analysis will then solve for the damped natural frequencies and mode shapes using the free-vibration equation at the motor shaft rotational speed of 1,800 RPM.

$$\mathbf{M}\ddot{\mathbf{u}} + (\mathbf{C} + \Omega\mathbf{G})\dot{\mathbf{u}} + \mathbf{K}\mathbf{u} = \mathbf{0} \quad (3.4.1)$$

5.6 Natural Frequencies and Mode Shape Summary

Table 5.6.1 lists the natural frequencies of the axially dominated and torsionally dominated modes of drive-train 2. The rigid-body modes are ignored in this analysis. Many of the axial modes share the same natural frequency as the torsional ones because they are the same mode. That is, the axial and torsional motions of the shafts are coupled. Lateral motions are also coupled and are included in the eigenvectors, but the axial and torsional motions were plotted at the request of the industrial owner.

Mode #	Axial Natural Frequency (Hz)	Torsional Natural Frequency (Hz)
1		0.36
2	2.13	2.13
3	2.28	2.28
4	2.61	2.61
5	3.73	3.73
6	4.61	4.61
7	11.13	11.13
9	16.82	16.82
17	41.12	41.12
23		74.12
43	257.67	
56	427.94	

Table 5.6.1. Natural Frequencies corresponding to axially dominant and torsionally dominant modes from the model

The algorithm for categorizing modes as axially, laterally, or torsionally dominant makes use of the normalization of the eigenvectors. Each eigenvector contains all 6 generalized displacements for each node, n , in the finite element model that are arranged in the following order: $z_n, x_n, y_n, \theta_{zn}, \theta_{xn}, \theta_{yn}$. Each eigenvector is multiplied by a scaling factor to set the magnitude of the maximum element to 1 and the other elements to have magnitudes between 0 and 1. Since the order of the degrees-of-freedom for each node in

the eigenvector is known, the program can determine which elements correspond to which degree-of-freedom. The analysis then scans each eigenvector and determines if the mode contains axial, lateral, or torsional components by checking if any of the values corresponding to these individual motions have magnitude greater than 0.01 (or within 1% of the maximum value).

The following plots show the 12 primary mode shapes for drive-train 2 corresponding to these natural frequencies. The axial components of the modes are shown on the left while the twist components are on the right. It is more convenient to illustrate the mode shapes in the form of 3-D plots because the magnitude and phase information for all nodes can be shown in one image. The axial locations of all shaft nodes, expressed in inches, are plotted along the axis labeled “Shaft Axis” to better illustrate the mode shapes and the distribution of node points. The magnitude of vibration at each node is indicated by the radius of its blue circle. The phase of each node relative to all the others may be obtained by the direction of the red lines originating from the node and ending at a point along its blue circle. In addition, green circles indicate transitions from the last node of one rotor to the beginning node of the next rotor. They are simply markers and do not indicate shaft vibration amplitude or phase. Because the drive-train 2 system model has 4 rotors, 3 green circles are shown because there are 3 shaft transitions. The following paragraphs describe the mode shapes as observed from their figures.

Mode 1, with a natural frequency of 0.36 Hz, has a dominant twist component relative to the axial one because none of the scaled axial components of any shaft node exceed 0.01. Figure 5.6.1 indicates rigid twist motion of the motor and bull gear shafts. Rigid twist motion also occurs for the pinion gear and compressor shafts, but with larger amplitude and in the opposite direction to that of the motor and bull gear shafts.

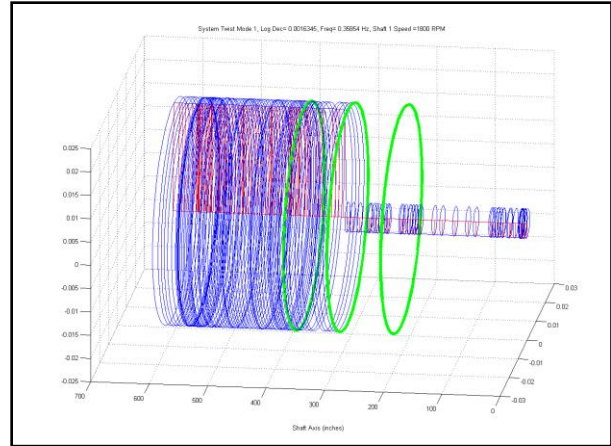


Figure 5.6.1. Mode 1. Freq= 0.36 Hz. Log Dec=0.0016

Modes 2 through 6 contains axial and twist components of motion that are roughly equal in magnitude as indicated by the scales of the axes in figures 5.6.2 through 5.6.6. The axial vibrations of the motor and bull gear shafts have the same amplitude but are slightly out of phase with respect to each other. The compressor shaft exhibits no axial motion and the pinion gear vibrates axially with much higher amplitude and nearly 180 degrees out of phase with respect to the motor and bull gear shafts. The twist motions of these modes are nearly identical to those of mode 1 except that the compressor shaft twists with slightly greater magnitude than the pinion gear shaft.

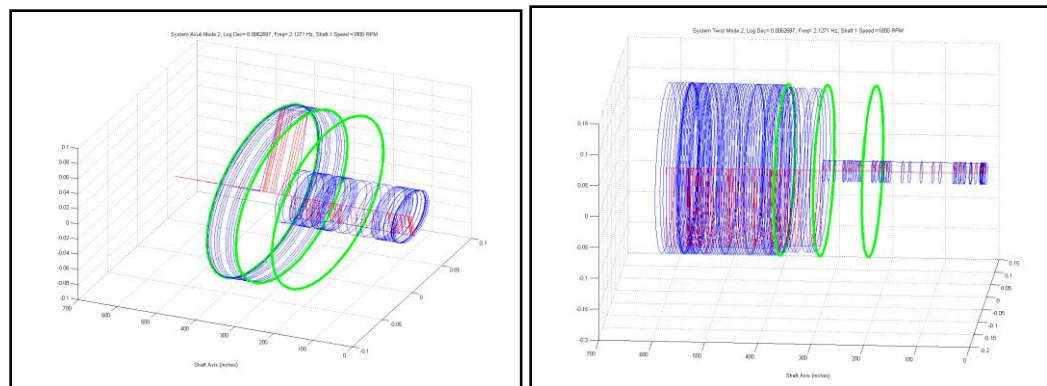


Figure 5.6.2. Mode 2. Freq=2.13 Hz. Log Dec=0.0063

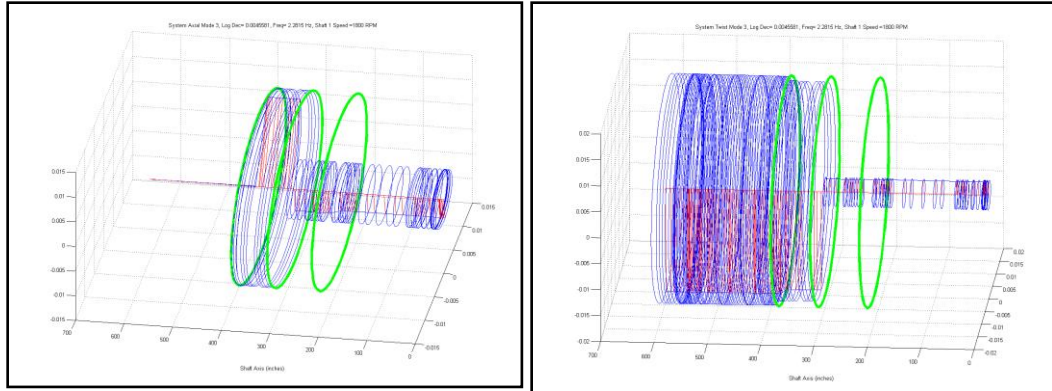


Figure 5.6.3. Mode 3. Freq=2.28 Hz. Log Dec=0.0046

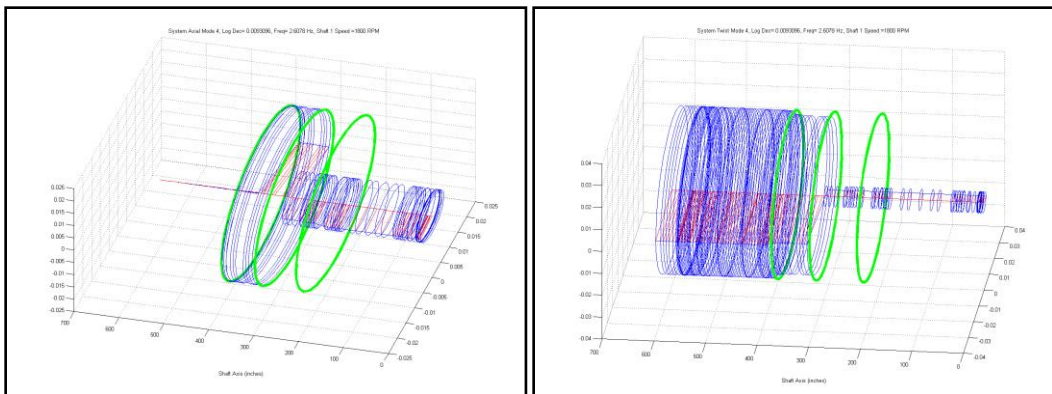


Figure 5.6.4. Mode 4. Freq=2.61 Hz. Log Dec=0.0093

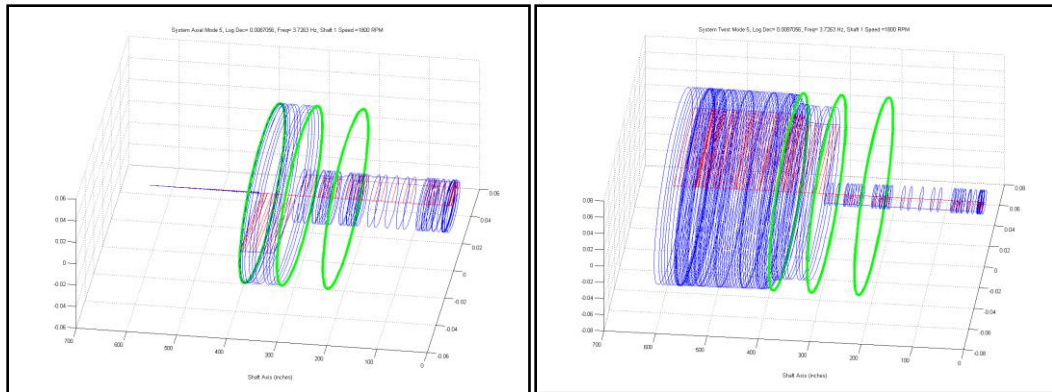


Figure 5.6.5. Mode 5. Freq=3.73 Hz. Log Dec=0.0087

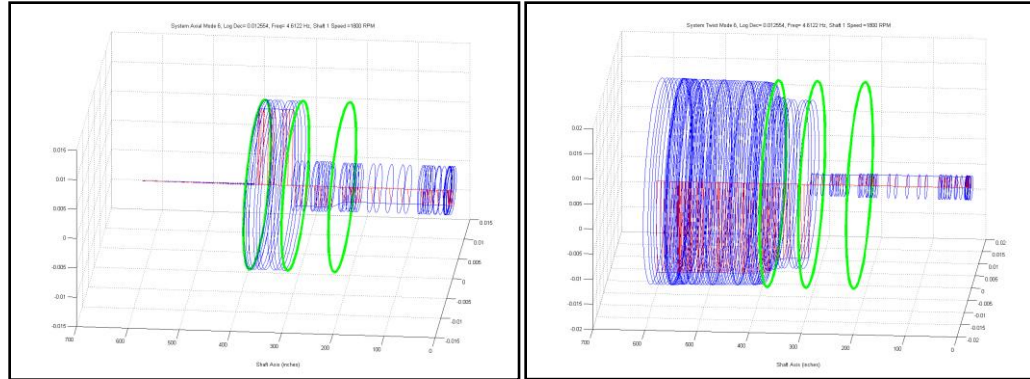


Figure 5.6.6. Mode 6. Freq=4.61 Hz. Log Dec=0.0126

Mode 7, in figure 5.6.7, has similar axial characteristics to those of the previous modes except that the non-free end of the compressor shaft is beginning to contribute more to the motion and the bull gear shaft moves with slightly greater amplitude than the motor shaft. The twist component of this mode however has greatly changed such that the compressor shaft exhibits almost all of the motion. The pinion gear twists with much smaller magnitude, and the bull gear and motor shafts vibrate negligibly.

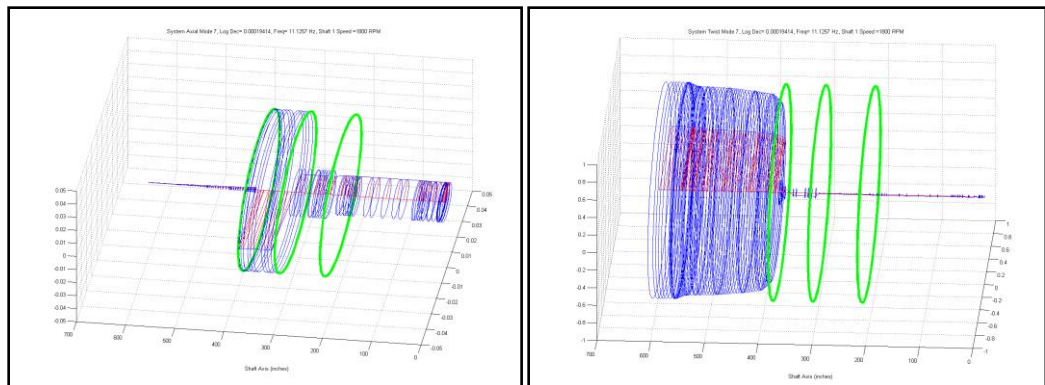


Figure 5.6.7. Mode 7. Freq=11.13 Hz. Log Dec=0.0002

Mode 9, in figure 5.6.8, illustrates the same axial vibration trend as expressed in the previous paragraph for mode 7. As with mode 7, the twist component is largely dominant as indicated by the scale of its plot. The motor shaft undergoes almost all of the twist motion

and the vibration is transferred to the bull gear shaft through the flexible coupling where the amplitude rapidly decays.

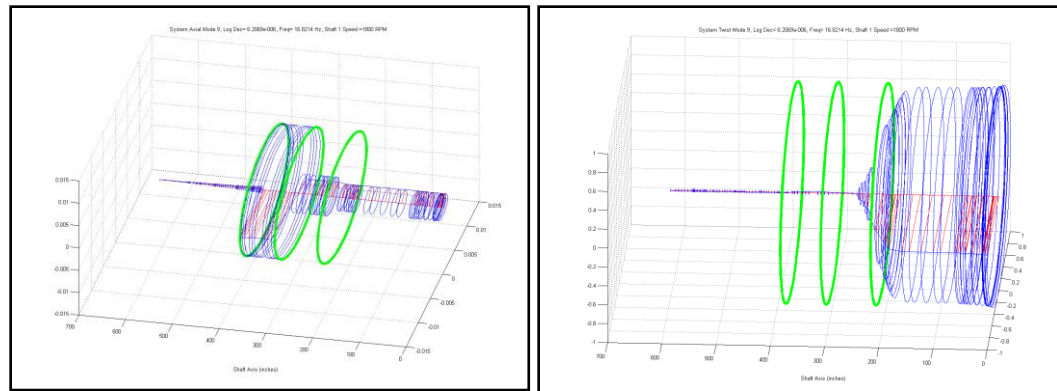


Figure 5.6.8. Mode 9. Freq=16.82 Hz. Log Dec=6.21E-6

Mode 17, shown below in figure 5.6.9, is a continuation of the same axial vibration trend as expressed in the previous two paragraphs. The motor shaft and the bull gear shaft both undergo rigid axial displacements but are approximately 90 degrees out of phase. In addition, the bull gear shaft moves axially with greater amplitude than that of the motor shaft. The pinion gear shaft vibrates rigidly with the largest amplitude, but is in the opposite direction to that of the bull gear shaft. The axial vibration of the pinion gear shaft is transmitted to the compressor shaft whereby it gradually decays along its length.

The twist component of mode 17 is nearly the same magnitude as that of its axial component. There is little motion throughout the motor shaft, but nearly uniform twisting develops along the bull gear shaft. The pinion gear shaft twists with much greater amplitude in the opposite direction to that of the bull gear shaft. Its amplitude quickly attenuates after the flexible coupling. The amplitude continues to decay along the compressor shaft until the location of the node point. The twisting amplitude gradually increases along the rest of the compressor shaft but 180 degrees out of phase with respect to the previous direction.

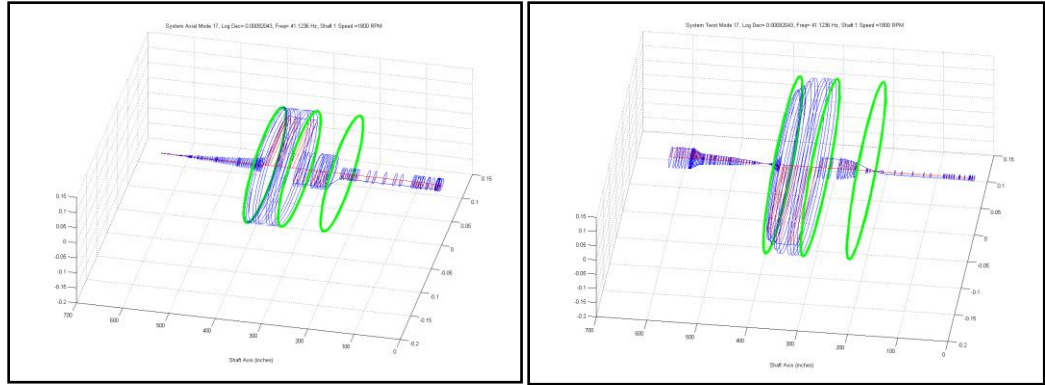


Figure 5.6.9. Mode 17. Freq=41.12 Hz. Log Dec=0.0009

Mode 23 is dominated by twist motions of the compressor shaft only as illustrated in figure 5.6.10. Some twist motion develops near the end of the pinion gear shaft and greatly increases in amplitude after the flexible coupling. The twist amplitude decays to a node point along the compressor shaft and subsequently increases with a 180 degree phase shift.

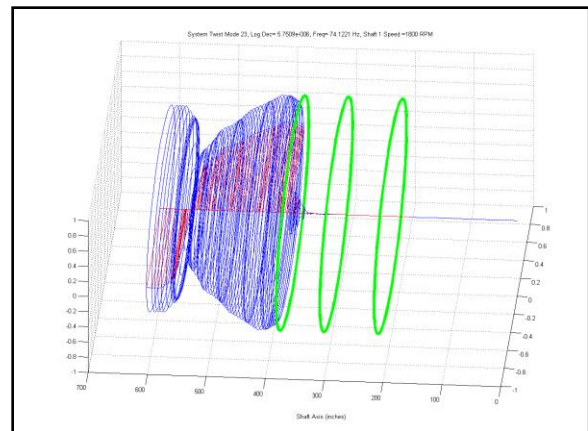


Figure 5.6.10. Mode 23. Freq=74.12 Hz. Log Dec=5.75E-6

Mode 43 is dominated by axial motions of the compressor shaft as shown in figure 5.6.11. Some axial motion develops along the pinion gear shaft and rapidly increases at the flexible coupling where a 90 degree phase shift occurs. The vibration decreases along the length of the compressor shaft and undergoes a gradual phase shift until the location of the

thrust bearing. At the thrust bearing, another 90 degree phase shift occurs and the amplitude and phase of the remainder of the compressor shaft remain uniform.

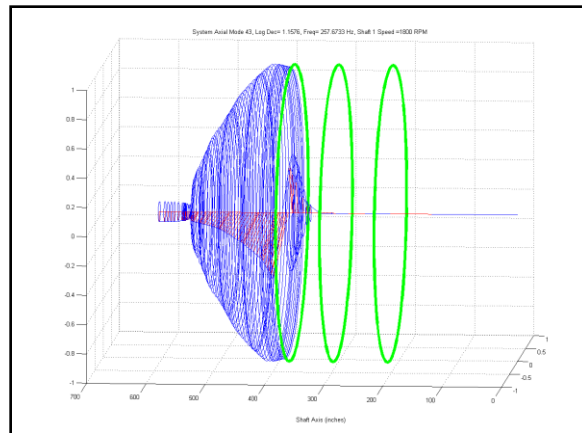


Figure 5.6.11. Mode 43. Freq=257.67 Hz. Log Dec=1.1576

Mode 56 is dominated by axial motion along the motor shaft as indicated in figure 5.6.12. The first node of the motor shaft experiences the greatest amplitude and the amplitude decreases along the subsequent nodes until the location of the node point of the mode. The amplitude gradually increases along the remainder of the motor shaft but has been shifted 180 degrees from the node point. After the flexible coupling, the amplitude decreases along the bull gear shaft and the rest of the shaft does not participate in the mode.

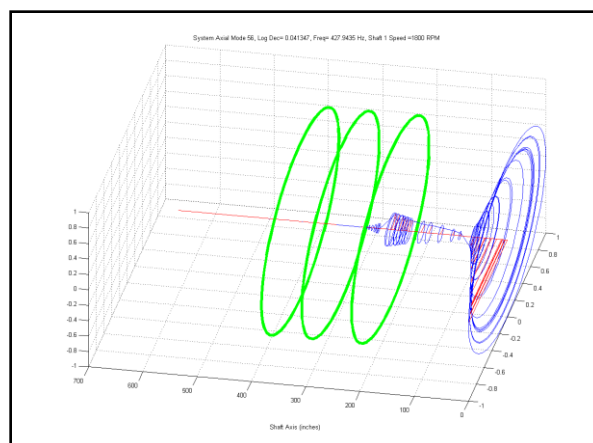


Figure 5.6.12. Mode 56. Freq=427.94 Hz. Log Dec=0.0413

5.7 Conclusion

The natural frequencies and mode shapes of drive-train 2 were evaluated at the motor shaft rotational speed of 1,800 RPM by solving the free-vibration equation with coupled degrees of freedom. The results of this analysis show reasonable similarities to the undamped torsional mode shapes and natural frequencies provided from the undamped torsional analysis. Table 5.7.1 summarizes the comparison of the natural frequencies between the torsional mode shapes of the coupled analysis and those of the strictly torsional analysis. Figures 5.7.1 through 5.7.3 show a comparison between the mode shapes of these two separate analyses and illustrate that they reasonably support each other.

Undamped Mode #	Natural Freq (Hz)	Current Mode #	Natural Freq (Hz)
2	14.22	9	16.82
3	44.76	17	41.12
4	71.27	23	74.12

Table 5.7.1. Comparison of torsional natural frequencies between the Undamped and Current models

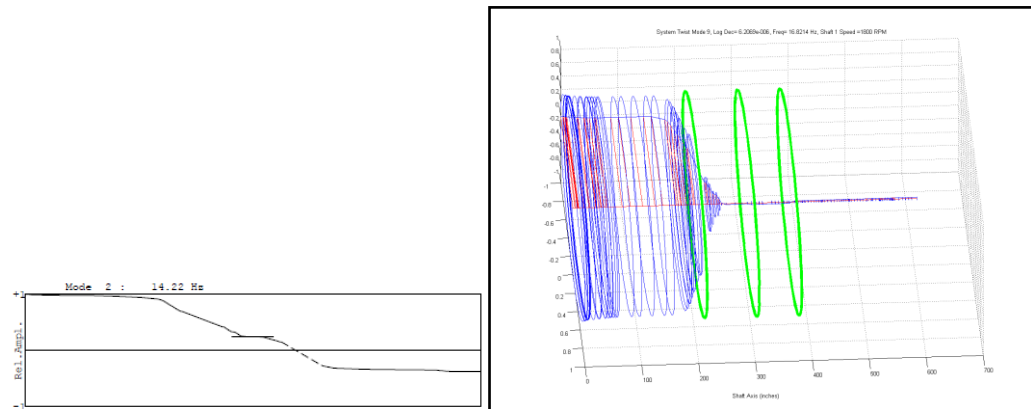


Figure 5.7.1. Twist comparison of Undamped mode 2 and current model mode 9

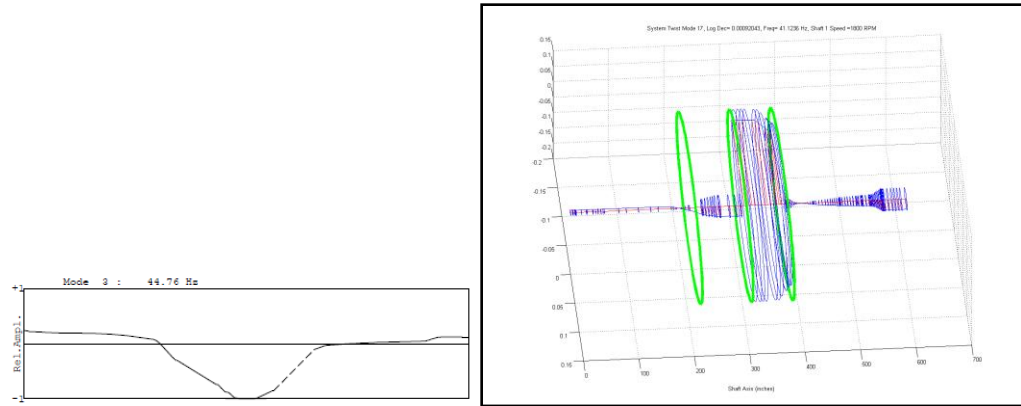


Figure 5.7.2. Twist comparison of Undamped mode 3 and current model mode 17

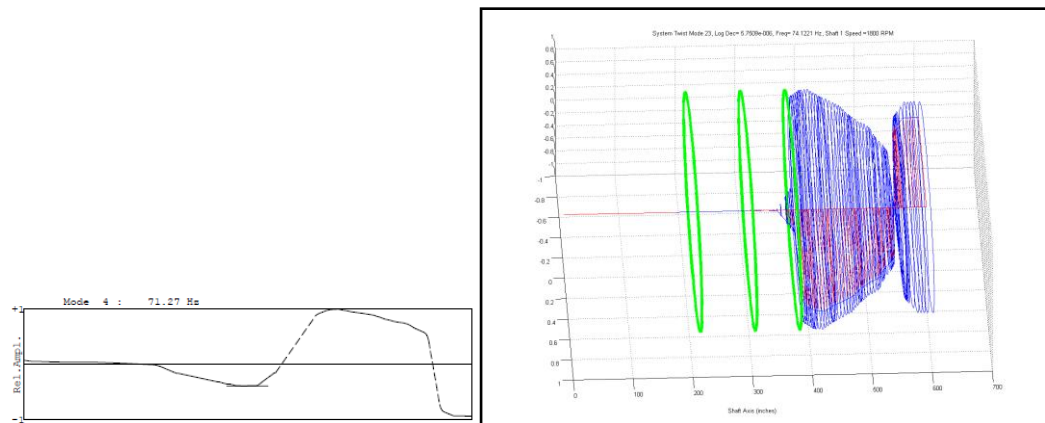


Figure 5.7.3. Twist comparison of Undamped mode 4 and current model mode 23

The advantage of running a coupled degree-of-freedom analysis over a strictly torsional, axial, or lateral one includes the ability to capture additional modes that show more complicated modal responses and therefore model the vibration of the geared rotating system more accurately. The first 6 modes conducted in this analysis were not captured from the strictly torsional analysis and may show potential low frequency instabilities. A summary of these modes and the potential instability are provided in the following paragraph.

The first 6 natural frequencies and mode shapes constitute low-frequency modes (less than 5 Hz) and have very similar axial and torsional components. The plots of these low-frequency modes suggest that the bull gear and pinion vibrate 180 degrees out of phase in both the torsional and axial directions. In addition, the low log decrement values suggest potential instability and thus a greater likelihood of the gearbox running noisy. It seems reasonable that most of the modes have low log decrement values because the relative axial motion of the shaft at the location of the thrust bearing is almost always very low. Mode 43 is the only exception to this trend and is therefore well damped. Therefore, the effective damping of the thrust bearing in most of the modes is minimal despite the large axial damping coefficient used in this analysis.

Additional sources of damping in this model stem from the radial bearings which may be ineffective if the lateral motion of the shaft is negligible at the bearing locations. Lateral mode shape plots would be necessary to verify this. This finite element analysis may be applied to multiple shaft systems with multiple gear stages and many additional features can be expected in future analyses such as: mode shape plots of lateral vibration and forced-response analyses due to tooth errors and time-varying mesh stiffness.

Chapter 6 Conclusions

6.1 Accomplishments

This thesis introduces modern methods of incorporating gear dynamics into geared systems using the finite element method. A gear mesh finite element model was produced and successfully incorporated into a general rotor dynamic finite element analysis that solves both free and forced vibration analyses.

The 12x12 stiffness matrix, originally developed by Stringer, provides the terms, in the rotor dynamic equations of motion, that couple the axial, lateral, and torsional degrees of freedom of the geared shafts. This 12x12 stiffness matrix is a function of the following: normal pressure angle, helical angle, face width, pitch radii, orientation angle, and gear elastic moduli. The average gear mesh stiffness, a parameter used in the stiffness matrix, is calculated from using the face width and the gear elastic moduli. The formula for tooth to tooth contact was originally provided by Spotts, but it was modified to account for the average number of tooth pairs in contact through one mesh cycle.

This formulation offers unique advantages that do not appear in the literature. One advantage is the applicability to both spur and helical geared systems. Another is the robustness to account for arbitrary angles of orientation within the plane of rotation of the connected shafts. The calculation for the average gear mesh stiffness requires minimal computation and remains reasonably accurate. Previous methods to determine the average gear mesh stiffness required more complex formulas or experimental data, which is time-consuming to acquire.

A finite element model of the herringbone gearbox of a steam-turbine generator drive-train application was developed in Chapter 4, and it illustrates some of the capabilities of these finite element analyses. Models for the low and high-speed shafts of the gearbox were constructed from Timoshenko beam elements, and the stiffness and damping coefficients for the original gearbox bearings were determined from a separate finite element analysis. The gear mesh stiffness matrix was produced using both material and geometric parameters of the gears and was modeled as the source of connectivity between the low and high-speed shafts. The suspected source of instability was modeled as cross-coupled stiffness acting at the node of the flexible coupling, and the results from the stability analysis showed that it was successfully reproduced. Subsequent finite element analyses of a new 3-lobe pressure dam bearing design indicated that it would eliminate the unstable mode and would retain the stability of all modes within the operating speed range across the range of generator load cases. Stability and unbalance response analyses of the gearbox with the new bearing design confirmed the recommendation to switch from the original gearbox bearings to the 3-lobe pressure dam ones, and the physical drive-train has been operating normally since.

The second application consisted of modeling a synchronous-motor-gearbox-compressor drive-train in Chapter 5. The objective was to determine its natural frequencies and mode shapes, and to assess their stability. An undamped torsional rotor dynamic analysis had been provided to compare its results to those of the current model. Models for the shafts, bearings, and couplings were easily integrated into the finite element global matrices in the form of mass, stiffness, gyroscopic, and damping matrices. The modeling was complete after adding the gear mesh stiffness matrix to the global stiffness matrix at the nodal locations corresponding to the gears on the low and high-speed shafts. Post-

processing of the results revealed the existence of several low-frequency modes that had questionable stability. The results of this stability analysis indicated that the current model can determine modes that individual non-coupled analyses would overlook.

6.2 Implications

The work accomplished in this thesis raises important implications for future models of gearbox dynamics. Gearbox modeling has increased in complexity as both computing power and memory availability continue to rise. This is reflected from the fact that the finite element method replaced both lumped parameter methods and the transfer matrix method in rotor dynamic analyses, which require substantially less computing power but are less accurate [32]. Modern uses of the finite element method, when applied to gears, focus on the stresses and displacements of gear bodies and are therefore useful for determining time-varying mesh stiffness properties. Most previous finite element analyses of geared systems, however, have either ignored the shaft and bearing contributions to the vibration behavior or have used simple approximations to model them [37]. Finite element models of shaft systems are becoming increasingly popular in solving rotor dynamics problems, and therefore, finding more ways to integrate the finite element analysis of gear teeth and gear bodies into rotor dynamic codes would yield not only greater accuracy in free vibration and forced response analyses but would produce better diagnostic tools for determining gear tooth errors.

6.3 Future work

Many improvements to the analysis of geared rotor systems can be expected. The current analysis calculates only the average tooth mesh stiffness over the mesh cycle. Incorporating the time-varying properties of the tooth mesh stiffness will be essential to producing more accurate models of geared rotor dynamics. This is especially true for forced-response analyses where the relative amplitude, phase, and frequency of the mesh forces, when compared to other forces, such as unbalance, may substantially alter the vibration results.

Additional sources of vibration include errors in tooth geometry that result in transmission errors. These transmission errors perturb the constant tangential velocity assumption at the pitch point for involute gear pairs. This often produces substantial vibration at the gear mesh that should not be ignored.

The current analysis ignores the effects of the thin film of lubricant separating the teeth of a gear pair at the pitch point. As the gear teeth move into and out of engagement, the film thickness varies with time during squeezing. The resulting time-varying pressure profile between adjacent teeth generates forces that act on the gears and are consequently transmitted to the geared shafts. An additional step in the analysis that couples the tooth elastic deformation to changes in the properties of the lubricant through temperature variation is desirable.

While accounting for each of these effects contributes to more accurate geared rotor dynamic analyses, they are secondary in importance when compared to the coupling of degrees of freedom. We can expect more accurate models of geared systems to emerge, and thus better methods to predict their dynamic behavior and to diagnose sources of instability in industrial drive-trains.

Bibliography

- [1] J.Ishikawa. 1951. Deflection of gear (in Japanese). *Trans Japan Soc. Mech. Engres* 17: 103-106
- [2] S.L. Harris. 1958. Dynamic loads on the teeth of spur gears. *Proceedings of the Institution of Mechanical Engineers* 172: 87-112.
- [3] D.C. Johnson. 1962. Modes and frequencies of shafts coupled by straight spur gears. *Journal of Mechanical Engineering Science* 4, 241-250.
- [4] G.V. Tordion. 1963. The mechanical impedance approach to the dynamics (torsional vibrations) of geared systems. *American Gear Manufacturers Association Paper* 209.04.
- [5] F. F. Ehrich. 1964. Shaft whirl induced by rotor internal damping. *Journal of Applied Mechanics* 23 (1): 109-115.
- [6] J.G. Bollinger and R.J. Harker. 1967. Instability potential of high speed gearing. *The Journal of the Industrial Mathematics Society* 17: 39-55.
- [7] F. F. Ehrich. 1967. The influence of trapped fluids on high speed rotor vibration, *Trans. ASME, J.Eng. Ind.* 89 (B) : 806-812.
- [8] J.A. Wolf. 1968. Whirl Dynamics of a Rotor Partially Filled with Liquid, *Trans. ASME, J. Appl Mech* 35(4): 676-682.
- [9] R. Kasuba. 1971. Dynamic loads on spur gear teeth by analog computation. *American Society of Mechanical Engineers Paper* 71-DE-26.
- [10] S. M. Wang and I.E. Morse. 1972. Torsional response of a gear train system. *Journal of Engineering for Industry, Transactions of the American Society of Mechanical Engineers* 94: 583-594.
- [11] D.B. Wallace and A. Seireg. 1973. Computer simulation of dynamic stress, deformation and fracture of gear teeth. *Journal of Engineering for Industry, Transactions of the American Society of Mechanical Engineers* 95: 1108-1115.
- [12] H. Fukuma, T. Furukawa and T. Aida. 1973. Fundamental research on gear noise and vibration (6th report, generation mechanism of radial and axial vibration of spur gears). *Bulletin of the Japanese Society of Mechanical Engineers* 16: 1094-1107.
- [13] S.M. Wang. 1974. Analysis of non-linear transient motion of a geared torsional. *Journal of Engineering for Industry, Transactions of the American Society of Mechanical Engineers* 96: 51-59.

- [14] H. Rettig. 1975. Vibrations in gear drives; test results and calculation method for dynamic tooth forces. *Proceedings of the International Federation of the Theory of Machines and Mechanisms 4th World Congress*, Newcastle.
- [15] M.W. Salzer. 1977. The dynamics of a layshaft gearbox. Ph.D. Thesis, Cambridge University.
- [16] S. Kiyono, T. Aida, and Y. Fujii. 1978. Vibration of helical gears 1—theoretical analysis. *Bulletin of the Japanese Society of Mechanical Engineers* 21: 915-922.
- [17] J.W. Daws. 1979. An analytical investigation of three dimensional vibration in gear-coupled rotor systems. PhD Dissertation, Virginia Polytechnic Institute and State University.
- [18] B. Kisher. 1979. Effect of gear errors on non-linear vibrations of a gear train system. *Proceedings of the International Federation of the Theory of Machines and Mechanisms Fifth World Congress*, Montreal, 1122-1125.
- [19] H. Black. 1979. Effects of fluid-filled clearance spaces on centrifugal pump and submerged motor vibrations, *Proceedings of the 8th Turbomachinery Symposium*, Texas A&M University: 29-38.
- [20] K.L. Wang and H.S. Cheng. 1981. A numerical-solution to the dynamic load, film thickness, and surface temperatures of spur gears: Part 1 Analysis. *Journal of Mechanical Design, Transactions of the American Society of Mechanical Engineers* 103: 177-187.
- [21] K.L. Wang and H.S. Cheng. 1981. A numerical-solution to the dynamic load, film thickness, and surface temperatures of spur gears: Part 2 Results. *Journal of Mechanical Design, Transactions of the American Society of Mechanical Engineers* 103: 188-194.
- [22] C. Troeder, H. Peeken, A. Laschet, and K. Tooten. 1983. Causes and effect of torque in hammering of toothed gears. *Proceedings of the International Federation of the Theory of Machines and Mechanisms 6th World Congress*, New Delhi, 2: 936-943.
- [23] L.D. Mitchell and J.W. Daws. 1983. A basic approach to gearbox noise prediction. *Society of Automotive Engineers Transactions* 9: 3366-3379.
- [24] R.G. Kirk, G.N. Donald. 1983. Design criteria for improved stability of centrifugal compressors. *Rotor Dynamical Instability, G00227, ASME*, New York: 59-71, June.
- [25] H. Lin, R.L. Huston, and J.J. Coy. 1984. Dynamic analysis of straight and involute tooth forms. *American Society of Mechanical Engineers Paper* 84-DET-226.
- [26] K. Umezawa, S. Sato, and K. Kohno. 1984. Influence of gear errors on rotational vibration of power transmission spur gears, 1. Pressure angle error and normal pitch error. *Bulletin of the Japanese Society of Mechanical Engineers* 27: 569-575.

- [27] F. Kucukay. 1984. Dynamic behavior of high speed gears. *Proceedings of the Third International Conference on Vibrations in Rotating Machinery, Institution of Mechanical Engineers*, 81-90.
- [28] T. Iwatsubo, S. Arii, and R. Kawai. 1984. Coupled lateral-torsional vibration of rotor system trained by gears (I. Analysis by transfer-matrix method). *Bulletin of the Japanese Society of Mechanical Engineers* 27: 271-277.
- [29] T. Iwatsubo, S. Arii, and P. Kawai. 1984. The coupled lateral torsional vibration of a geared rotor sytem. *Proceedings of the Third International Conference on Vibration in Rotating Machinery, Institution of Mechanical Engineers*, 59-66.
- [30] A.W. Lees. 1984. Dynamic loads in gear teeth. *Proceedings of the Third International Conference on Vibrations in Rotating Machinery, Institution of Mechanical Engineers*: 73-79.
- [31] M.F. Spotts. 1985. *Design of machine elements, 6th edition*. Englewood Cliffs, NJ: Prentice-Hall, Inc.
- [32] S. V. Neriya, R. B. Bhat, and T. S. Sankar. 1985. Coupled Torsional-Flexural Vibration of a Geared Shaft System Using Finite Element Analysis. *Shock and Vibration Bulletin* 55: 13-25.
- [33] S. V. Neriya, R. B. Bhat, and T. S. Sankar. 1985. Vibration of a geared train rotor with torsional-flexural coupling. *American Society of Mechanical Engineers Paper* 85-DET-124.
- [34] K. Umezawa, S. Sato, and K. Kohno. 1985. Influence of gear error on rotational vibration of power transmission spur gear, 2. Waved form error. *Bulletin of the Japanese Society of Mechanical Engineers* 28, 2143-2148.
- [35] H. Ota, Y. Ishida, A. Sato, and T. Yamada. 1986. Experiments on vibration of a hollow rotor partially filled with liquid, *Bull. JSME* 29 (256): 3520-3529.
- [36] J.C. Nicholas. (1986-1990). Stabilizing turbomachinery with pressure dam bearings. *Encyclopedia of Fluid Mechanics*, 2 1-18.
- [37] H.N. Ozguven, and D.R. Houser. 1988. Mathematical Models Used in Gear Dynamics –A Review. *Journal of Sound and Vibration* 121: 383-411.
- [38] H. N. Ozguven. 1991. A non-linear mathematical model for dynamic analysis of spur gears including shaft and bearing dynamics. *Journal of Sound and Vibration* 145(2): 239-260.
- [39] A. Kahraman, H.N. Ozguven, D.R. Houser, and J.J. Zakrajsek. 1992. Dynamic analysis of geared rotors by finite elements. *ASME Journal of Mechanical Design* 114: 507-514.

- [40] J.S. Rao, J.R. Chang, and T.N. Shiau. 1995. Coupled Bending-Torsion Vibration of Geared Rotors. *ASME DE-Vol. 84-2, Design Engineering Technical Conferences*, Vol. 3, Part B: 977–989.
- [41] Y. Cai. 1995. Simulation on the rotational vibration of helical gears in consideration of the tooth separation phenomenon (a new stiffness function of helical involute tooth pair). *Journal of Mechanical Design, ASME* 117 (3): 460-469.
- [42] Z. Luo and X. Sun. 1996. Coupled torsional-lateral-axial vibration of a geared shaft system using substructure synthesis. *Mechanism and Machine Theory* 31 (3): 345-352.
- [43] F.F. Ehrich. 1999. *Handbook of Rotordynamics*, Krieger Publishing Co, Inc.
- [44] T. Yamamoto, Y. Ishida. 2001. *Linear and Nonlinear Rotordynamics. A Modern Treatment with Applications*, John Wiley & Sons, Inc.
- [45] Chien-Hsing Li, Hong-Shun Chiou and Chinghua Hung, et al. 2002. Integration of finite element analysis and optimum design of gear systems. *Finite elements in analysis and design* 38 (3): 179-192.
- [46] J. Lin, and R.G. Parker. 2002. Mesh stiffness variation instabilities in two-stage gear systems. *Journal of Vibration and Acoustics, ASME* 124(1): 68-76.
- [47] Axial and centrifugal compressors and expander-compressors for petroleum, chemical and gas industry services : Downstream segment (2002). (7th ed., July 2002 ed.). Washington, D.C: American Petroleum Institute.
- [48] J. Brauer. 2004. A general element model of involute gears. *Finite elements in analysis and design* 40(13-14): 1857-1872.
- [49] J. Wang and I. Howard. 2005. Finite Element Analysis of High Contact Ratio Spur Gears in Mesh. *ASME Journal of Tribology* 127: 469- 483.
- [50] D.B. Stringer, P.N. Sheth, P.E. Allaire. 2007. A Twelve Degree-Of-Freedom Gear-Mesh Stiffness Matrix for Helical and Spur Gears for Rotor Dynamics. ROMAC Report No. 523.
- [51] J.A. Chaudhry. 2008. Rotor dynamics analysis in MatLab framework. Charlottesville, VA: University of Virginia.
- [52] D.B. Stringer, P.N. Sheth. 2009. Geared Rotor Dynamic Methodologies for Advancing Prognostic Modeling Capabilities in Rotary-Wing Transmission Systems. ROMAC Report No. 545.
- [53] S. Chowdhury. 2010. Effect of shaft vibration on the dynamics of gear and belt drives. PhD Dissertation from Ohio State University. UMI Dissertation Publishing.

- [54] W. Sun, T. Chen, and X. Zhang. 2011. A new method to calculate bending deformation of involute helical gear. *U.P.B. Science Bulletin, Series D* 73 (3): 17-30.